An Integrated Physical Model Characterizing Planetary Atmosphere and Heat

by
Koen Vogel PhD
Published December 06, 2022

An integrated physical model characterizing planetary magnetism and heat

ABSTRACT

Planetary magnetic fields are commonly thought to be generated by a dynamo, whose convection cells convert thermal and mechanical energy to magnetic energy via induced electric currents. Dynamo theory however can only speculatively explain most planetary magnetic field strengths and geometries, does not take into account or explain planetary heat flow or anomalies, and has very limited predictive value. A more evident, alternative theory requiring substantially fewer assumptions is derived from the Solar System's planets' magnetic and thermal data: the planetary magnetic fields are generated by a Solar Wind Induced Electromagnet (SWIEM), whose byproduct is substantial waste heat. This newly proposed model better explains the existence, magnitude and stability of the Earth's dipolar and non-dipolar fields, as well as its current polarity. It clarifies the origins of Earth's fluid Outer and solid Inner Core, and offers credible mechanisms for geomagnetic excursions and reversals, dipole strengthening and weakening, westward secular non-dipole drift, and solar signals in the geomagnetic power spectrum. It accounts for the areas of high surface heat flow that originate in the Outer Core, and thereby establishes a credible link between the geomagnetogenic process and continental drift. The SWIEM model rationalizes the magnetic field geometry and heat anomalies of "problematic" planets such as Saturn and Neptune, and accurately predicts planetary magnetic field strengths from best-estimate input data.

INTRODUCTION

Physical processes that are able to distribute and focus energy on planetary scales are rare, so planetary data sets that show significant spatial covariation – such as Earth's geomagnetic and geothermal data - strongly suggest that a single process is responsible for their shared geometry. The characterization of such a process – its underlying physical model - usually relies on relatively easily-acquired Earth data, but is often improved by the analysis of extra-terrestrial data. The prime test of any theory or model is whether it can reasonably explain all observations, and whether it can be used to accurately predict future observations. The characterization of planetary processes therefore necessitates the evaluation of their physical models against the physical, chemical and geological observations of all planets.

Only in the best case can the analysis of a single planetary data set verify a theory: for example, the analysis of reflection and refraction data of P and S waves originating from large earthquakes provides convincing evidence of Earth's high-density liquid Outer (OC) and a solid Inner (IC) Cores (Stacey & Davis 2008; Tkalčić & Phạm 2018). More often however the analysis of a single planetary data set can only outline a large and highly uncertain solution space that requires further refinement via the integration of other sets: for example, the heat flow at the Earth's Core-Mantle boundary (CMB) is optimally determined from a physical Earth model that integrates surface heat flow, radioactive mineral decay times and distributions, seismic velocity models, metamorphic mineral occurrences and transition depths, etc. (Verhoogen 1980).

The magnetic fields of all planets in our solar system - and most of their satellites - are commonly thought to be generated by an internal dynamo, whose convection cells convert thermal and mechanical energy to magnetic energy via induced electric currents (Stanley

2014). The theory however cannot satisfactorily explain most planetary magnetic field geometries, must rely on numerous power source and internal planetary geometry assumptions that are contradicted by observations, does not take into account or explain planetary heat flow or anomalies, and has very limited predictive value. This article develops an alternative theory that draws inspiration from the magnetic fields of Jupiter's Galilean satellites, and that integrates all relevant planetary physical, chemical and geological data. The theory better explains the existence, magnitude and stability of Earth's dipolar and non-dipolar fields, as well as its current polarity. It clarifies the origins of Earth's fluid Outer and solid Inner Cores, and offers credible mechanisms for geomagnetic excursions and reversals, dipole strengthening and weakening, westward secular non-dipole drift, and solar signals in the geomagnetic power spectrum. It accounts for most of the areas of high surface heat flow - such as plate margins and hotspots - that originate in the OC, and thereby establishes a credible link between geomagnetogenesis and continental drift. The theory's underlying physical model can be used to accurately predict the equatorial magnetic field strengths of Earth, Jupiter, Saturn, Uranus, and Neptune from best-estimate input data, and to explain the magnetic field geometry and heat anomalies of "problematic" planets such as Saturn and Neptune.

THE GEOMAGNETIC POWER SOURCE

Planetary processes distribute and focus large amounts of energy on planetary scales. A large, fairly steady-state – yet still enigmatic - energy source on the order of 3.6-10 TW (Verhoogen 1980) has been powering the Earth's geomagnetic field for billions of years. The field is commonly believed to be continually generated in Earth's fluid OC, whose estimated temperature is likely far above its Curie value (Merrill et al. 1998). Neither the OC nor the IC are therefore likely to be permanently magnetized (Merrill et al. 1998), indicating that any magnetogenic energy source must be constant enough to continually power the field over billions of years, yet variable enough to effect the observed changes over shorter time periods. Little consensus exists among present-day authors on the dominant geomagnetogenic power source, and Merrill et al. (1998) caution that "all calculations and relevant observational data on this subject contain a sufficient number of problems". Some authors (e.g. Verhoogen 1980) claim "an embarrassing abundance of riches" of possible candidates (despite the many highly speculative assumptions that are often required) and show a reluctance to pick a favorite, while others (e.g. Gubbins et al. 2003 and this article) arrive at a preferred candidate via an attrition process.

The Covariation of Geothermal and Geomagnetic Data

An OC energy source likely powers both the geomagnetic field as well as the estimated 4 TW of heat lost by the Core to the Mantle via the Core-Mantle Boundary (CMB) (Verhoogen 1980; Merrill et al. 1998). Most energy forms readily convert to heat, but the reverse is a highly inefficient process: for example, a thermal dynamo's efficiency is likely on the order of 10-20% (Verhoogen 1980; Merrill et al. 1998). Therefore, a large percentage of the energy of any magnetogenic process should be observable as its waste heat signature. An integrated approach towards better characterizing the process consequently takes both thermal and magnetic data - and their evident spatial and temporal covariation (Fig. 1) - into account.

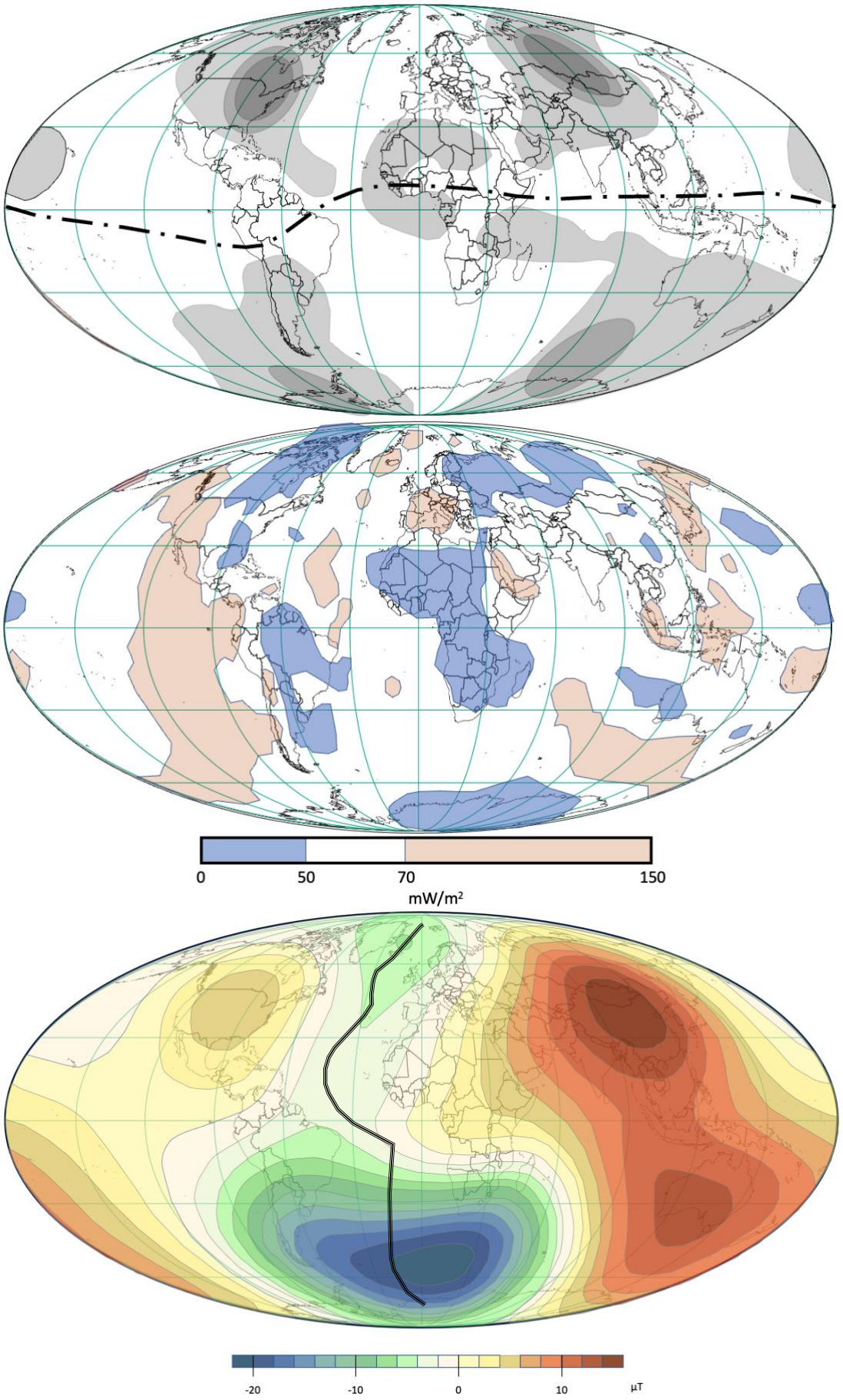

Figure 1: (top) 1690 to 1990 average of the radial component of the geomagnetic field squared (B_r^2) at the core surface (after Gubbins & Love 1998; darker areas are higher; dot-dash line is magnetic equator); (middle): the spherical harmonic expansion (to degree 36) of conductive heat flow (after Hamza et al. 2007); (bottom): Magnitude of the 1995 non-dipolar field (after Lühr 2000); black line represents the mid-Atlantic ridge.

The Northern Hemisphere (NH) has two geomagnetic non-dipole (radial geomagnetic energy) highs centered around 55° N latitude and 90° W and 100° E longitude resp., locations that coincide with surface heat flow lows (Fig. 1). Both locations are in the center of their continental plates, remote from any hot or active plate margins, and form the bullseye of oblong radial field strength and heat flow contours that are neatly bisected by the mid-Atlantic ridge heat anomaly that follows the geomagnetic non-dipole field strength saddle between the two highs (Fig.1 bottom; ~90° long. separation from each high). An argument can be made that a relatively thick continental crust results in a lower surface heat flow than a thinner oceanic crust, but this cannot explain why – in a hemisphere that is ~60% covered by ocean – the geomagnetic non-dipole highs are located at the center of continental plates. No plausible feedback mechanism exists between the geomagnetogenic OC process and crustal composition or thickness, so the observed NH geomagnetic and geothermal geometries are likely caused by a single process that focusses radial magnetic energy (±20% of the energy) at the center of continental plates while focusing waste heat at the plate margins (±80% of the energy), thereby – at least partially – also driving continental drift (Verhoogen 1980). Such reasoning could also explain why continental drift is absent on Earth's sister planet, Venus, whose magnetic field is possibly non-existent (Smrekar et al. 2014).

In the Southern hemisphere (~80% covered by ocean) the non-dipole locations are also close to land and remote from hot plate boundaries, though the case is not as convincing as its northern counterpart. Nevertheless, both geothermal lows (Fig. 1 middle) and historical radial field strength highs (Fig. 1 top) lie on roughly the same meridians as their northern counterparts. The 90° W and 100° E longitude lines also roughly coincide with the preferred virtual geographic pole (VGP) trajectories during recent magnetic reversals: transitional VGP paths are strongly biased to lie in the American 90° W meridian or its antipodal direction (McFadden & Merrill 1995; Gubbins & Love 1998; Merrill et al. 1998), again demonstrating the strong spatial correlation between geothermal and geomagnetic data.

Equatorial heat flow lows are centered on North Africa and the mid-Pacific Ocean, once again evidently remote from hot plate boundaries, and unrelated to crustal composition.

Planetary (dis)similarities

The observed magnetic fields of Earth, Jupiter, Saturn, Uranus and Neptune are highly similar, so – as a working hypothesis – are assumed to be generated by a unique magnetogenic processes powered by similar energy sources. This is not a huge leap of faith: the Maxwell equations indicate electric currents are the only known source of magnetic fields, and only very few planetary processes can be contemplated that can generate and focus the necessary electrical energy on planetary scales. Some similarities and dissimilarities between the planetary fields:

- They can be modelled as largely dipolar fields with magnetic axes roughly perpendicular to the planet's orbital plane, that is roughly perpendicular to the solar direction, suggesting that solar energy plays a role in the magnetogenic process. Planetary dipole tilts range from relatively small (Earth, Jupiter, Saturn) to large (Neptune: 47°, Uranus: 59°). Uranus' rotational axis roughly lies in its orbital plane (Kivelson & Bagenal 2014), so its relatively large field strength suggests that Coriolis forces or rotational torque – for example between a fluid mantle and a solid core – only have minor to absent roles in the magnetogenic process.

- They can be highly axisymmetric (Saturn), somewhat axisymmetric (Jupiter, Earth), or non-axisymmetric (Uranus, Neptune) (Kivelson & Bagenal 2014; Stanley 2014), indicating the magnetogenic process is able to produce a wide range of magnetic field geometries.
- Their strength roughly varies with day length (rotation speed) and planet size (Stacey & Davis 2008; Kivelson & Bagenal 2014): large planets with shorter days (Jupiter) have stronger fields than small planets with longer days (Mercury). Planets with extremely long days (Mercury, Venus) show small to absent fields.
- The chemical compositions of the terrestrial planets (Mercury, Venus, Earth, Mars) differs significantly from those of the gas giants (Jupiter, Saturn, Uranus, Neptune) (Kivelson & Bagenal 2014; Weissman 2014), suggesting that chemical composition does not play a significant role in the magnetogenic process. For example: radioactive mineral content is unlikely to play a major role as the planet with the strongest field (Jupiter) likely has the lowest radioactive mineral content (Marley & Fortney 2014).
- Earth and Venus are compositionally similar (Weissman 2014), yet only Earth has a measurable magnetic field. Both have a rigid crust and hot spot volcanism, that is volcanism caused by upwelling mantle plumes driven by radial heat and density gradients (Smrekar et al. 2014). Yet Earth's geologic processes are largely dominated by plate tectonics: large curvilinear heat anomalies that originate in the OC (e.g. the mid-Atlantic ridge) drive Earth's plate movements (Verhoogen 1980). The absence of plate tectonics and curvilinear anomalies on Venus has been speculatively attributed to a higher rigidity of its basaltic crust (Smrekar et al. 2014), yet a more likely explanation is that Earth's geomagnetogenic process is also responsible for its curvilinear heat anomalies, and that both are absent on Venus.

Earth-Internal Magnetogenic Power Source Candidates

A thermal dynamo requires planet-internal heat gradients that drive its convective fluid motions. Note that some authors favor mechanical dynamos, where convection is (partially) driven by density gradients. The main problem with all Earth-internal power candidates is that they are fundamentally diffuse in nature, so require a process that continually focuses the energy when generating the long-lived steady-state geomagnetic field and the long-lived heat anomalies (such as the mid-Atlantic ridge) that originate in the OC (Steinberger 2000; Burke 2011). As Verhoogen (1980) states: "A structureless, formless, isotropic sea of heat is geologically useless"; he identifies four Earth-internal power candidates:

- "Original" heat from the Earth's formation
- Tidal dissipation of kinetic energy (tidal friction)
- Gravitational energy released through crystallization of the Inner Core
- Radioactivity

Original Heat

A geomagnetogenic OC process powered by the Earth's original heat, that is heat generated from the gravitational energy released during the Earth's formation, would decay due to Ohmic dissipation in a few tens of thousands of years (Verhoogen 1980; Merrill et al. 1998; Stacey & Davis 2008). Original heat can only still be a major component of Earth's present-day heat flow if conduction, not convection, has been the main form of heat transfer

(Verhoogen 1980), which is incompatible with a thermal dynamo driven by convection. Observations indicate that planetary surface heat flow is negatively correlated to magnetic field strength: planets with low surface heat flow, such as Uranus and Neptune still support relatively strong magnetic fields, while planets with high surface heat flow, such as Mercury and Venus, have weak to possibly absent fields (Stanley 2014). Kelvin-Helmholtz modelling indicates Saturn's magnetic field cannot be powered by original heat as it effectively lost all its internal heat over 2 billion years ago (Marley & Fortney 2014). In addition, local planetary surface heat anomalies such as Earth's mid-Atlantic ridge, or Neptune's warmer south pole (Roman et al. 2020) are incompatible with a presumably radially-symmetric original heat flow loss.

Conclusion: unlikely magnetogenic energy source

Tidal dissipation of kinetic energy (tidal friction)

Estimates of the power derived from the tidal dissipation of the Earth's kinetic energy due to the gravitational pull of the Sun and Moon are on the order of 10^{-4} TW, which is several orders of magnitude too low to power the geomagnetic field (Verhoogen 1980; Ruff & Anderson 1980; Dehant & Van Hoolst 2014). While tidal forces likely play a large role for the internal heat budgets of planetary satellites, the reverse is unlikely: the Moon is only roughly 1.25% of the mass of the Earth, and the satellite systems of Jupiter, Saturn, and Uranus each contain roughly 0.01% of the mass of their respective planets (Weissman 2014).

Conclusion: unlikely magnetogenic energy source

Gravitational energy released through crystallization of the Inner Core

The main argument against latent/gravitational energy released through the crystallization of the Inner Core is that a liquid OC and solid IC imply a lower-than-adiabatic temperature gradient through a stratified Core, which in turn is incompatible with a geodynamo driven by thermal convection (Verhoogen 1980; Stacey & Davis 2008). Recent studies have demonstrated that only a small fraction of such gravitational energy is available to drive convection (Gubbins et al. 2003). Furthermore, it is very unlikely that the planet with the strongest field, Jupiter, with a liquid metallic hydrogen mantle and solid iron-rich core (Kivelson & Bagenal 2014; Marley & Fortney 2014) would have a similar process.

Conclusion: unlikely magnetogenic energy source

Mechanical/compositional Dynamo

The estimated density of the OC suggests that a significant percentage of lighter elements, such as Sulphur, are lowering its specific gravity (Gubbins et al. 2003; Stacey & Davis 2008). Some authors therefore believe chemical convection, a variant of the gravitational geodynamo whereby the solidification of the IC releases these light elements, drives the OC convection through buoyancy effects (Merrill et al. 1998; Gubbins et al. 2003; Stacey & Davis 2008). However, in the long term such a mechanism results in a stratified core: the lack of a return flow of light elements would - over billions of years - result in the stratification of the OC into a low-density outer OC shell surrounding a higher-density inner OC and IC, which is not in evidence (Tkalčić & Phạm 2018). Compositional convection is an energetically diffuse and inefficient convection mechanism, requires numerous compositional

and physical assumptions not in evidence, and would not produce long-lived surface-observable heat features such as the mid-Atlantic ridge or a warmer Neptune south pole (Roman et al. 2020). This mechanism is mostly Earth-specific, and therefore very unlikely to power similar convections in the gas giants, though some workers believe similar mechanisms could power the Mercury, Saturn, and Ganymede dynamos (Stanley 2014).

Conclusion: unlikely magnetogenic energy source

Radioactivity

The main argument against a radioactive heat source powering the magnetogenic process is that radioactive minerals are strongly oxyphilic, and were therefore likely enriched in the Earth's Crust but depleted in its Mantle and Core during the Earth's differentiation into layers: the differentiation of the liquid metallic OC is thought to require severely reducing conditions that are incompatible with the relatively high radioactive mineral concentrations required to power a geodynamo (Verhoogen 1980; Stacey & Davis 2008). Radioactive heat source models must therefore assume an undifferentiated primal chondritic OC mineralogy rich in radioactive elements which is not in evidence (Verhoogen 1980; Stacey & Davis 2008). Furthermore, it is unlikely that other planets such as the gas giants would show similar enrichment in their cores: Jupiter has a core that is similar in size to Earth's but a magnetic field that is an order of magnitude larger, while Saturn has a significantly larger core than Earth's but a field strength that is lower (Marley & Fortney 2014). Venus is chemically similar to Earth but has no measurable magnetic field (Smrekar et al. 2014)

Conclusion: unlikely magnetogenic energy source

Planet- and Satellite-Internal Energy Sources

The relatively simple dipolar magnetic field geometries of the other planets and satellites in our solar system require complex - and often highly speculative – energy sources under dynamo theory (Stanley 2014). A variety of existentially uncertain magnetogenic energy sources could plausibly power other-worldly dynamos, though the assumptions under which their energies are sufficient are often contradicted by observations. A summary of the current hypotheses (Stanley 2014):

- Mercury: magnetic field geometry is unexplainable under a "standard" dynamo; energy source thought to be Sulphur buoyancy in an iron-sulfide fluid core
- Venus: possibly absent magnetic field; suggested reason for the absence of an active dynamo is the lack of convection, which in turn is attributed to "insufficient" core cooling due to a "different mode of mantle convection"
- Jupiter: magnetic field geometry can be modeled by a "standard" dynamo; unclear energy source (possibly original heat) speculatively causing convection in a hypothetical outer shell of its metallic hydrogen mantle (Kivelson & Bagenal 2014)
- Saturn: an axisymmetric field that cannot be generated by a "standard" dynamo (Cowling's theorem; Merrill et al. 1998); convection attributed to negative buoyancy of speculative "Helium Rain" falling through its metallic hydrogen mantle
- Uranus and Neptune: magnetic field geometry cannot be caused by a "standard" dynamo; unclear energy source speculatively causing convection in a hypothetical mantle shell of liquid water-ammonia-methane

- Ganymede: dipolar field that is anti-parallel to Jupiter's field; dynamo assumed to be gravitationally driven by "iron snow" solidifying at its outer fluid core boundary, in addition to magnetic flux from Jupiter's field (Collins & Johnson 2014)
- Europa and Callisto: magnetic fields are demonstrably powered by the magnetic flux generated during the satellites' movements through Jupiter's inclined magnetic field (Zimmer et al. 2000; Collins & Johnson 2014)

Under dynamo theory a wide range of speculative energy sources and existentially uncertain processes are somehow able to focus disperse energy, organize electrical currents on a planetary scale, and generate highly similar dipolar magnetic fields in often speculative fluid shells. However, many of the energy candidates' sole piece of existential evidence is the presence of a planetary magnetic field. The sole demonstratable power source – the magnetic flux generating Europa and Callisto's magnetic fields – is planet external.

Often a planet-internal low-conductivity ocean is inferred to be the source (salt water oceans on Europa and Callisto, water-ammonia-methane ocean in Uranus and Neptune, shell of metallic hydrogen on Jupiter) despite the fact that similar conductivity oceans on Earth do not generate planet-wide fields and show large departures from spherical symmetry in their conductance (Kushinov, 2008). Such speculative low-conductivity low-magnetic-permeability internal planetary oceans are highly unlikely dynamo sources: their low conductivity (typically 1-10 $S.m^{-1}$) ensures that any significant magnetic energy generation will be accompanied by enormous amounts of waste heat.

Conclusion: Proposed planet-internal energy candidates are unlikely magnetogenic power sources

Summary

The previous sections have demonstrated that all plausible planet-internal energy sources are unlikely magnetogenic power sources: they could power a geodynamo under various – often highly speculative - assumptions, yet often their physical existence and magnitude are highly uncertain, and most are contradicted by widely-accepted physical Earth models. Recent work has demonstrated that none of the Earth-internal thermal candidates are suitable, and doubts thermal convection is driving the geodynamo (Gubbins et al. 2003). The efficiency of a geodynamo is low (between 10-20%; Verhoogen 1980; Merrill et al. 1998), indicating that large amounts of energy are required to effect even small amounts of geomagnetic change, which is recognized as the main challenge of the geodynamo dynamic modelers (Aubert & Finlay 2019). All Earth-internal candidates are likely to be relatively constant over sub-millennial timescales: even the most variable, for example radioactive decay, only varies significantly over extremely long periods, as the half-lives of the most common radioactive isotopes (U-235, U-238, Th-232, K-40) are on the order of billions of years (Ruff & Anderson 1980; Stacey & Davis 2008). This steady nature is in fact a requirement of the geodynamo: any Earth-internal source needs to be continuous enough to power the relatively steady-state geomagnetic field over billions of years, yet variable enough to effect significant changes over sub-millennial time scales, as the OC is likely unable to permanently store magnetic energy. This strongly argues for an Earth-external magnetogenic power source.

All Earth-internal energy candidates are diffuse in nature, while a steady-state geodynamo's convection cells require a steady-state temperature or density gradient. It is extremely

unlikely that Earth-internal diffuse heat sources can focus energy for prolonged periods of time, for example concentrate heat at the mid-Atlantic ridge for millions of years, as any heat concentration results in thermal gradients that advect heat away in an attempt to homogenize the OC temperature. Even convection caused by the crystallization of the IC only effects a radial temperature gradient, and cannot laterally focus heat on Earth. There is therefore strong evidence that this focused heat is a by-product of the magnetogenic process and not its cause.

THE GALILEAN SATELLITE'S EXTERNAL MAGNETOGENIC POWER SOURCE

Galileo flybys of Europa and Callisto provided clear evidence that their magnetic fields are induced: their dipole fields are consistently anti-parallel to the ambient Jovian field, as is predicted by the Maxwell equations for an induced field (Khuruna et al. 1998; Kivelson et al. 2000; Zimmer et al. 2000). The main power source of these fields is therefore demonstrably the magnetic flux generated during their orbit through Jupiter's inclined and rotating field: their induced magnetic fields display the apparent rotation (synodic) frequency of Jupiter (11.23 h for Europa and 10.18 h for Callisto; Zimmer et al. 2000). If a perfectly conductive shell covered the surface of these satellites, then the induced field, B_I, would exactly cancel out Jupiter's magnetic field, B_J, at the two points on the shell where the two fields are exactly anti-parallel to one another, that is where B_J is normal to the shell, at the dipoles of the induced field (Parkinson 1983).

Zimmer et al. (2000) derive an equation that correlates the instantaneous induced field, B_A, produced by a spherical shell of arbitrary conductivity (that is less than infinite conductivity) at time t, to the induced field of a perfectly conducting sphere:

$$B_A\,(t) = A.\,B_I(t - \frac{\phi}{f}) \qquad \text{(Eqn. 1)}$$

whereby A is an amplitude scaling factor, f the frequency of the primary field (B_J) oscillation, and ϕ is a phase shift (the induced field always lags behind B_J). Note that an important yet obscure role is played by the skin depth, the travel distance through the satellites' mantle at which the amplitude of the primary or induced field falls to 1/e of its original value: if the spherical inductor shell of arbitrary conductivity lies within the satellite, then both the primary and induced field will suffer energy losses ($A < 1$) while travelling through the mantle layers. The flyby data indicate that both Callisto and Europa can be accurately modelled as perfectly conducting spheres ($A \simeq 1$; $\phi \simeq 0$; Zimmer et al. 2000), indicating that energy losses due to mantle absorption of the primary (incoming) and induced (outgoing) electromagnetic energy are small.

Zimmer at al. (2000) demonstrate that a model whereby a hypothetical salt water shell inductor ($\sigma = 2.75$ S.m^{-1}) that sits just below the satellite's surface fits the magnetic field observations well. Note that this solution is non-unique - numerous other models may fit the magnetic data equally well – and that it is questionable whether such a shallow salt water shell is the optimal solution. For example, on Earth similar-conductivity salt water oceans fail to generate such planet-wide induced fields that perfectly counter-balance the diurnal geomagnetic flux or generate planet-wide magnetic fields (Kuvshinov 2008). A section below demonstrates that while a shallow salt water ocean inductor may theoretically fit the magnetic observations, its low conductivity ensures that any significant magnetic energy generation will be accompanied by enormous energy losses due to waste heat generation ($A<<1$), that is heat energy that is multiple orders of magnitude larger than the observed radiated heat. Only

ferromagnetic inductors, such as the satellites' cores, have both conductivity and magnetic permeability values that are consistent with low magnetogenic heat energy losses, though Zimmer at al. (2000) reject such models: their skin depth model predicts that a deep metallic core inductor would result in severe attenuation (A=0.125), and would therefore poorly match the magnetic observations (Khuruna et al. 1998). A discussion below demonstrates that Zimmer at al.'s skin depth model over-estimates electromagnetic (EM) mantle attenuation.

The magnetic field of Ganymede shows many similarities with the fields of Callisto and Europa: its dipole moment is also antiparallel to the ambient field of Jupiter, and induction signatures are also observed (Collins & Johnson 2014; Kivelson & Bagenal 2014), indicating that magnetic flux energy demonstrably plays a role in its field generation, though the location of the inductor and how its induced field contributes to its intrinsic field are unclear. Ganymede's magnetic field forms its own mini-magnetosphere within Jupiter's encompassing magnetosphere, and is purportedly (Stanley 2014) generated in its core by a self-sustained mechanical dynamo driven by negatively buoyant "iron snow" solidifying at the outer fluid core boundary. Recent models however indicate that while Ganymede could have had convective motion in its fluid core early in its history, its core is now stable against convection: its core cannot be the location of a magnetogenic dynamo (Collins & Johnson 2014). In addition, it remains unclear how a dynamo-generated field in an as yet unidentified fluid layer can combine with Ganymede's induced field to generate a field that strongly resembles an induced field.

The great compositional similarity of these satellites and their magnetic fields geometries begs the question: under what physical model could these similar fields be generated by similar processes and similar energies? The Callisto and Europa energy source – magnetic flux – would have to fully power Ganymede's induced field. But such energy would be attenuated during its travel through Ganymede's rock and ice mantle before reaching its inductor, which evidence suggests is its solid ferromagnetic core. Similarly, a high-conductivity metallic core is far more likely inductor than a salt-water shell for Callisto and Europa's induced fields, though the Zimmer et al. skin depth model predicts severe attenuation of both the primary and induced fields, while the observations suggest a maximum attenuation of only 30% ($A > 0.7$). It is therefore clear that a unified Galilean magnetogenic physical model can only be contemplated if the magnetogenic power source is magnetic flux, and the EM energy absorbed by the satellites' mantles is much lower than modelled: a unified Galilean satellite magnetogenic model can only exist if prevailing skin-depth models greatly overestimate EM attenuation. A section below demonstrates that such is likely the case.

PLANET-EXTERNAL ENERGY SOURCES

The similarity of the planetary magnetic fields – and Occam's razor – suggest the working hypothesis that all are generated by a unique magnetogenic process powered by similar energy sources. The analysis of the Galilean satellite data therefore suggests external magnetic flux is the power source inducing all planetary and satellite magnetic fields.

Solar energy is the only plausible Earth-external energy source able to supply the 3.6-10 TW (Verhoogen 1980) necessary to power the geomagnetic field, though a mechanism whereby such energy reaches the OC is not obvious. A solar energy source would clarify a number of observations that are otherwise difficult to explain:

- The temporal coincidence of geomagnetic dipole strength maxima with the Oort, Wolf, and Maunder solar activity minima (see below)
- The covariance of geomagnetic data with solar cycles: geomagnetic power spectral lines cluster around 21.4 years (sunspot cycle; Currie 1973) and 27 days (solar rotation cycle; Banks 1969); geomagnetic jerks occur with 10-year intervals (sunspot cycle; De Michelis et al. 2005); geomagnetic variability covaries with solar wind strength (Crooker et al. 1977; Stamper et al. 1999)
- The dipole axes of all planetary magnetic fields are roughly perpendicular to the solar direction (Kivelson & Bagenal 2014).

Solar Irradiation

The total Earth-incident solar radiation is on the order of 170 10^3 TW (Chen 2011), which is numerous orders of magnitude larger than the geomagnetogenic requirement. Much of this energy is however reflected by the Earth's atmosphere and surface, and the energy that is absorbed only penetrates to a maximum crust depth on the order of 10's of meters, even when converting to heat (Chen 2011). This high-frequency EM energy therefore does not reach the OC.

Conclusion: unlikely magnetogenic energy source

Solar Wind

The solar wind consists of a stream of charged particles (primarily protons and electrons) that is ejected from the Sun's corona at supersonic speeds, and is accompanied by stream-embedded magnetic energy (Kivelson & Bagenal 2014; Weissman 2014). The solar wind continually deforms the planetary magnetospheres, compressing their windward, dayside direction into a bow lobe, and extending their leeward, nightside into a tail lobe (Fig. 2; Crooker et al. 1977; Stamper et al. 1999; Kivelson & Bagenal 2014; Weissman 2014). The deformation process thereby generates magnetic flux, in a manner very similar to the flux generated by the movement of Callisto and Europa through Jupiter's inclined magnetic field. The average Earth-incident solar wind power of 5 TW (Dessler 1974; Herman & Goldberg 1978) is similar to the estimated 4 TW of heat lost by the OC to the Mantle (Verhoogen 1980; Merrill et al. 1998), as well as the estimated 3.6-10 TW (Verhoogen 1980) necessary to power the geomagnetic field, indicating it is a plausible candidate if a mechanism exists that transfers the energy to the OC without significant attenuation.

Other factors in this candidate's favor include:

- No assumptions are required: the solar wind evidently exists and its magnitude can be accurately estimated from best-estimate input. The solar wind continually deforms all planetary magnetospheres, thereby generating magnetic flux and demonstrably transferring solar wind energy to magnetospheres.
- It varies with solar cycles, and covaries with secular geomagnetic variability (Crooker et al. 1977; Stamper et al. 1999).
- Observed planetary magnetic field strength varies as a function of incident solar wind power, which therefore can be used to accurately predict planetary magnetic field strength (see below)

Conclusion: solar wind generated magnetic flux is the most likely planetary magnetogenic power source.

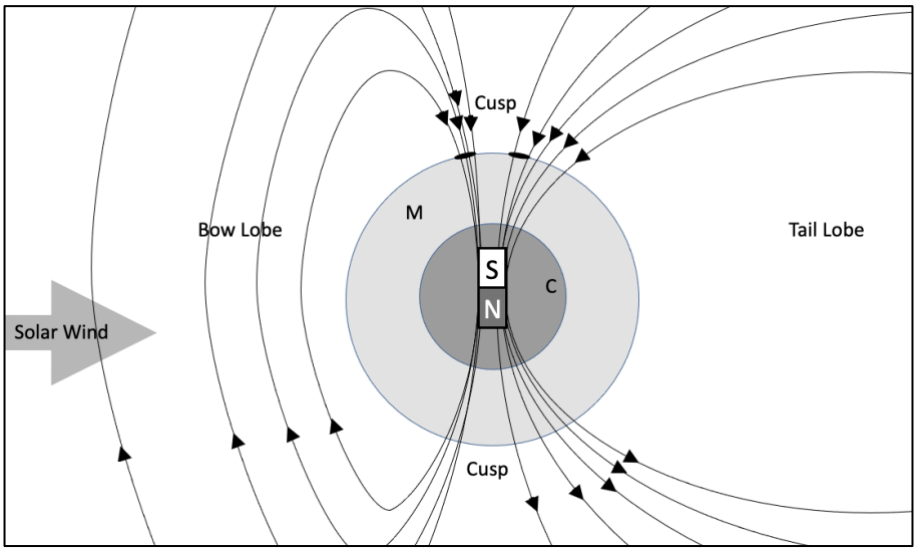

Figure 2: Schematic of how the Solar Wind deforms the geomagnetic field lines. C: Core; M: crust + mantle; Black ellipses in the Northern Hemisphere represent magnetic flux patches. Not to scale.

DIURNAL SOLAR WIND GENERATED MAGNETIC FLUX

A planetary magnetogenic process powered by the daily solar wind generated magnetic flux and its induced currents can be derived from the Galilean magnetogenic model outlined above. The following sections trace the Earth-incident solar wind energy from the edge of the Earth's magnetosphere – the magnetopause – to the OC, where the Maxwell equations indicate it induces the geomagnetic field.

The Maxwell equations

Electromagnetic (EM) energy interactions are governed by the Maxwell equations:

$$\nabla . \mathrm{D} = \rho_V \quad \text{(Eqn. 2)}$$

$$\nabla . \mathrm{B} = 0 \quad \text{(Eqn. 3)}$$

$$\nabla \times \mathrm{E} = F_E = -\frac{\partial B}{\partial t} \quad \text{(Eqn. 4)}$$

$$\nabla \times \mathrm{H} = F_M = \frac{\partial D}{\partial t} + \mathrm{J} \quad \text{(Eqn. 5)}$$

whereby $\nabla .$ is the divergence operator, D the electric flux density, ρ_V the electric charge density, B the magnetic flux density, $\nabla \times$ the curl operator, E the electric field, F_E the electromotive force, F_M the magnetomotive force, t time, H the magnetic field, and J the electric current density (Purcell & Morin 2013).

Eqns. 2 and 3 deal with field divergence. Eqn. 2 - Gauss' Law – states that an electric field diverges due to an electric charge (units of ρ_V are Coulomb/m^3). Eqn. 3 is Gauss' Law for magnetic fields, and states that magnetic fields never diverge away from a point: in contrast to the electric domain, magnetic charges and magnetic monopoles do not exist.

Eqns. 4 and 5 deal with the curls of electric and magnetic fields, that is how these fields circuit. Eqn. 4 – Faraday's law – indicates that a magnetic field that changes in time induces a circuiting electric field. Note that the negative sign in Eqn. 4 symbolizes a direction: a temporal change in magnetic flux density induces a circuiting electric field able to move charges (current), whose magnetic field in turn opposes the initially varying magnetic field (Lenz law). Alternatively, Eqn. 4 states that a circuiting electric field induces a change in magnetic flux density that will counteract the circuiting field. This illustrates the yin/yang behavior of the electric and magnetic fields: a disturbance in one gives rise to a perturbation in the other that will try to undo the original disturbance. The word "induces" - whereby one disturbance creates the other - may therefore be somewhat inappropriate. "Co-exist" or "accompany" may actually describe the situation better: either both or neither are observed.

Eqn. 5 indicates that both a time-variant electric flux as well as an electric current give rise to a circuiting magnetic field. This in essence explains the origin of all steady-state planetary magnetic fields: planet-interior currents must continually be generating their (circuiting) magnetic fields. Eqns. 4 & 5 suggest that these magnetogenic currents also circuit in a steady-state magnetic field, as a non-circuiting current would cause local charge build-up, which over time would reverse the current. Planet-internal electrical circuits are therefore inducing circuiting planetary magnetic fields.

The solar wind-magnetosphere energy exchange

The solar wind continually deforms the Earth's magnetosphere, compressing its windward, dayside direction into a bow lobe, and extending its leeward, nightside into a tail lobe (Fig. 2), thereby transferring its kinetic and magnetic energy to the magnetosphere as geomagnetic flux. The most commonly-used approach to calculating the energy exchange between the solar wind and a planet's magnetosphere is to use the work-energy principle, that is to consider the solar wind as tiny particle masses that collide with and transfer their kinetic and magnetic energy to the magnetosphere (Dessler 1974; Herman & Goldberg 1978; Baker et al. 1997). While numerically correct such an approach masks the physical mechanisms underlying the energy exchange, and as a result makes it more difficult to track where solar wind energy goes. A better approach is therefore to use Poynting's theorem (Purcell & Morin 2013), which describes the conservation of energy for electromagnetic fields. The Poynting vector, S, describes the power density (the flow of energy per time per area):

$$\mathrm{S} = \frac{\mathrm{E}\times\mathrm{B}}{\mu} \qquad \text{(Eqn. 6)}$$

whereby μ is the magnetic permeability of the medium. Note that the magnetic permeability of space (also referred to as the vacuum permeability), $\mu_0 = 1.256.10^{-6}\ \mathrm{N{\cdot}A^{-2}}$, which is > 0.

Poynting's theorem is a restatement of the conservation of energy: for a specified volume the rate of energy transfer, $\frac{\partial \mathcal{U}}{\partial \mathrm{t}}$, equals the rate at which fields do work on the charges in the volume, J.E, plus the energy flow leaving the volume (divergence of S).

$$-\frac{\partial \mathcal{U}}{\partial \mathrm{t}} = \nabla.\,\mathrm{S} + \mathrm{J}.\,\mathrm{E} \qquad \text{(Eqn. 7)}$$

The charged solar wind particles' (protons, electrons, alpha particles, etc) movement into the geomagnetic field results in a force acting on the particles that is perpendicular to the electric and magnetic fields, and therefore in their deflection (Eqn. 6; Fig. 3). Ambient geomagnetic field energy is hereby converted into deflected particle kinetic energy, while incident particle kinetic and magnetic energy is transferred to the magnetosphere as geomagnetic flux (Eqn. 7; Fig. 3). Magnetic flux is defined as the surface integral of the normal component of the magnetic field, so Fig. 3 demonstrates that the solar wind compression of the magnetosphere conceptually increases the magnetic flux density in F_2 at time t_1 relative to time t_0. This change in magnetic flux density must be accompanied by ("induces") an electric current somewhere in the magnetosphere (Eqn. 4); the following sections demonstrate that this current is very likely induced in the OC. Note that the solar wind deformation of the magnetosphere causes both positive (F_2) and negative (F_1) fluxes, whose distributions determine the location and direction of the co-existing (induced) electric currents.

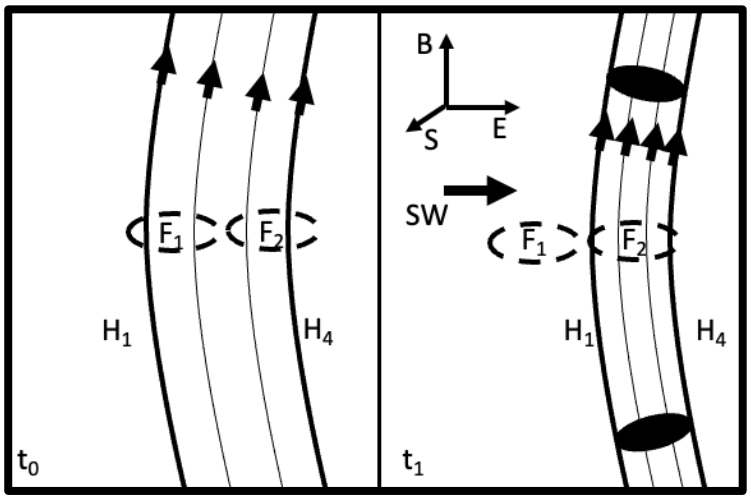

Figure 3: Schematic of how the solar wind compresses magnetic field lines on the bow side of a magnetosphere. SW: solar wind; H: magnetic field (H_1 and H_4 are field lines; B=μH); E: electric field. S: Poynting vector. F_1 and F_2 space-stationary flux patches. Left: time=t_0, before SW impact; Right: time=t_1, after SW impact

The Earth's diurnal geomagnetic variations: the solar quiet

For high-level discussion purposes the following conventions are used: the Northern (NH) and Southern (SH) hemispheres respectively lie to the North and South of the magnetic equator; LT 12:00 (local time noon) represents the meridian whereby the Sun is directly overhead, while LT 06:00, 00:00 and 18:00 refer to the meridians / positions resp. 90°, 180°, and 270° to the west of the LT 12:00 meridian. Magnetic fields are represented using oriented field lines that for a given location describe the direction of the magnetic force on a north monopole: on Earth they therefore currently flow out of the SH and into the NH (Fig. 2,3). Increases / decreases in the number of field lines per unit area signify resp. positive / negative magnetic flux densities.

The solar wind transfers its energy to the magnetosphere as geomagnetic flux. Its strength varies with time, so the average of the 5 days of lowest (quiet) monthly geomagnetic variations – termed the Solar Quiet (S_q) - best represents the steady-state Earth-incident solar wind energy (Fig. 4), which will be shown to be the main geomagnetogenic power source. The solar wind compresses the geomagnetic field lines on Earth's dayside (Fig. 3) and displaces them towards the poles (Fig. 2), that is its pressure "pushes" them away from the Sun. This is evidenced by the daily path of the North Magnetic Pole (NMP) position - the

intersection of the Earth's surface with the geomagnetic field line that vertically penetrates it - which follows an ellipse with axes of up to 80 km (Fig. 5b; Geological Survey of Canada 2008). A space observer will witness a stationary magnetospheric compression on the windward, dayside of the Earth, but an observer rotating with the Earth will notice local geomagnetic field variations that roughly follow a wave (Fig. 4, 5a). The maximum compression – and greatest negative geomagnetic field variation - occurs roughly at LT 12:00 (local time noon), when the Sun is directly overhead, while the minimum compression – and greatest positive variation – occurs at LT 24:00 (local midnight) when the Sun is directly on the opposite side of the Earth (Fig. 4). Magnetic flux is defined as the surface integral of the normal component of the magnetic field, so field lines that penetrate the Earth's surface at a high angle, that is lines in the polar regions (inclination > 70°) experience more flux variation than the equatorial regions (inclination ≈ 0°). Note that Fig. 4 roughly represents the NH summer solstice (Sun roughly over the Tropic of Cancer) so the magnetic flux at the north pole is at its yearly maximum, while the south pole is at its yearly minimum.

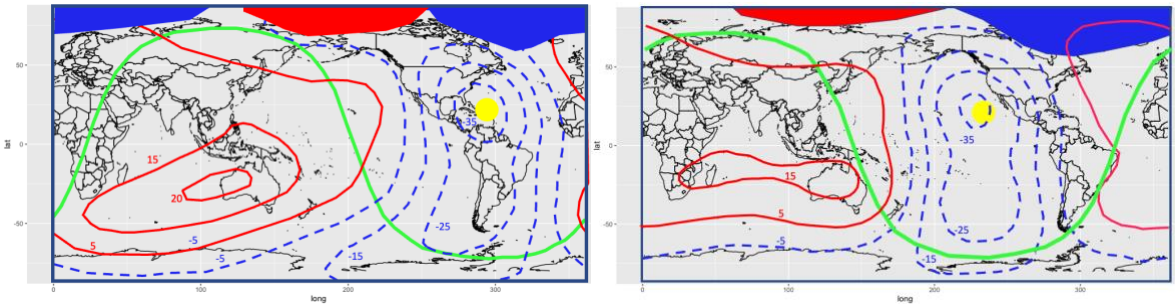

Figure 4: magnetic daily variation contours of the *Sq* total intensity (in nT) above the ionosphere at 16:30 UT (left) and 20:30 UT (right) derived from CHAMP satellite data (after: Turner et al. 2007). Colored Arctic blobs represent high positive (red) and negative (blue) magnetic flux areas. Yellow circle is solar direction; green line is the daylight boundary.

Fig. 4 represents the daily S_q magnetic variations near the top of the atmosphere, which represent the combination of the solar wind deformation of the magnetosphere (pressure) and the geomagnetic field's response (induced counter-pressure). The direct-incident solar wind particles consume the most geomagnetic energy and therefore effect the largest negative daily geomagnetic field strength variation: the largest negative contours occur at the Local Time (LT) 12:00 meridian (Fig. 4 left: ~308°; right: ~248°) when the sun is directly overhead. The maximum magnetic flux density generated by the solar wind therefore occurs in a high-latitude LT 12:00 "sweet-spot". As the Earth rotates, the direct-incidence location moves relatively westwards, and the sweet-spot magnetic flux density will decrease as the location rotates relatively eastwards: the maximum rate of flux density change (dB/dt) occurs at the polar LT 12:00 positions, where the trend flips from increasing to decreasing.

Due to the Earth's rotation during the course of the day the direct-incidence location moves relatively to the west, while the locally deformed meridians move relatively to the east (Fig. 5c). As the deformed meridians rotate eastwards the solar wind pressure and its transferred magnetic flux start to decrease, the magnetospheric deformation becomes less, and the geomagnetic field exerts less counterpressure, and the geomagnetic field starts to "recover". Full recovery occurs near the LT 18:00 position (Fig. 4 left: 38°; right: 338°), whereby the solar wind generated magnetic flux density returns to 0, and the negative magnetic flux of the recovering geomagnetic field (Fig. 4 blue blobs) reaches a maximum (Fig. 5a). As these locations rotate further eastwards, they will enter the magnetotail, where geomagnetic field extension (negative compression) occurs, with a maximum negative magnetic flux density occurring at LT 24:00. The further rotation of these locations from LT 24:00 to LT 12:00 then follows the mirror sequence: the geomagnetic field recovers from its extension near the

LT 06:00 position (Fig. 4 left: 218°; right: 158°), where the deformation contours return to 0 (Fig. 5a) and the positive magnetic flux of the recovering geomagnetic field (Fig. 4 red blobs) reaches a maximum (Fig. 5a).

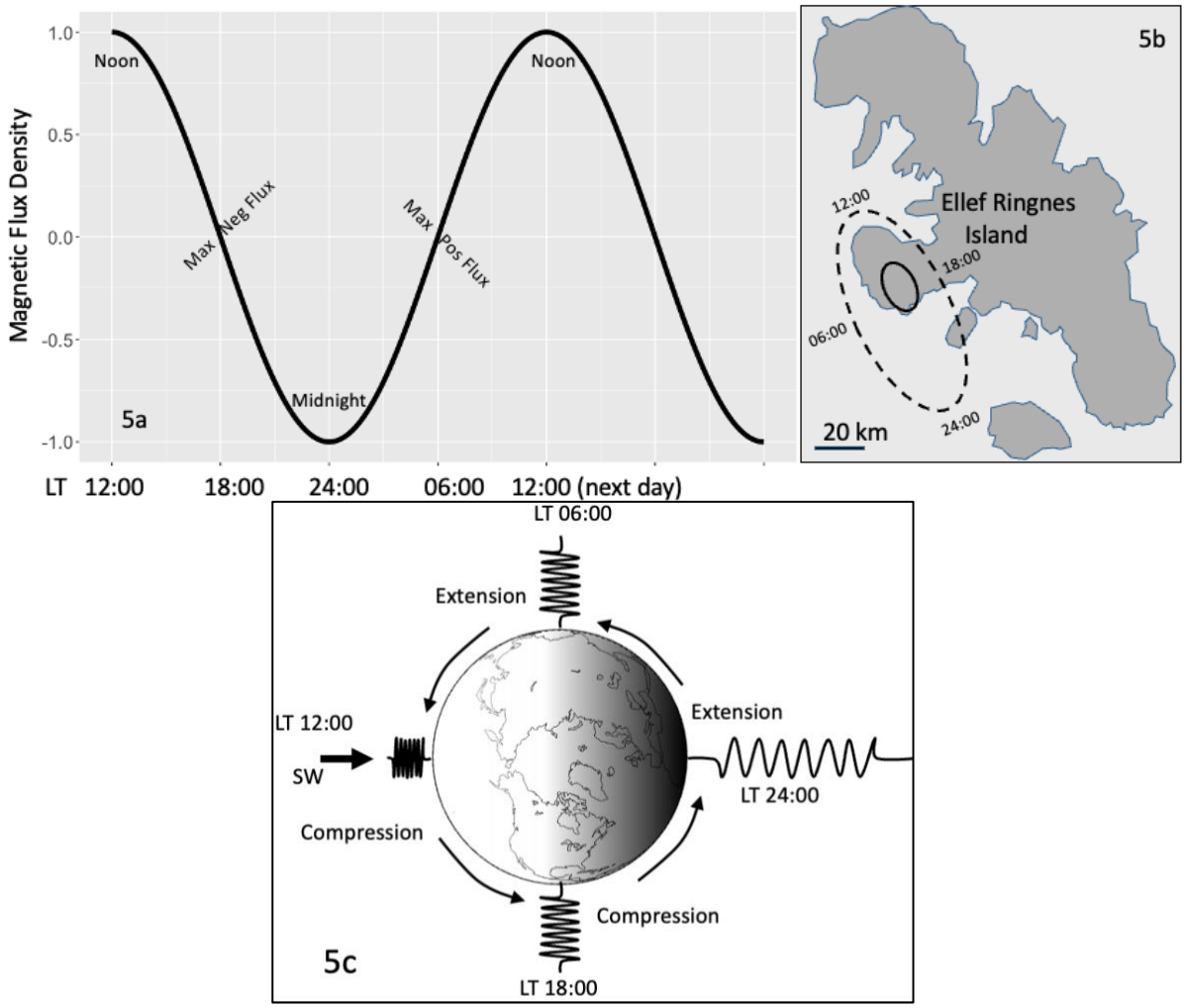

Figure 5: a) Normalized solar wind generated magnetic flux density during idealized local diurnal compression of the geomagnetic field as viewed by an observer on Earth; b) daily path of the North Magnetic Pole (NMP) in 1991 (after Geological Survey of Canada 2008): small solid ellipse represents "quiet" days of low solar wind; large dashed ellipse represents the path during more active days. Numbers reflect LT at the position. c) Daily compression and extension of the geomagnetic field by the solar wind represented as a coiled spring.

The deformation process is conceptually similar to a rotating spring: the spring is compressed (stores flux energy) at LT 12:00, but releases this energy by LT 18:00; the spring is extended at LT 24:00, but releases this energy by LT 06:00. The diurnal geomagnetic flux energy generated by the solar wind therefore propagates as a three-dimensional electromagnetic wave (Fig. 4 & 5), a geomagnetic flux pulse with an extremely low frequency f roughly equal to $(1/24\ h * 3600\ s.h^{-1})^{-1} \approx 10^{-5}$ Hz (Fig. 5a).

The physical location of the Solar Wind Induced Currents (SWICs)

The analysis above indicates that the daily S_q deformation of the magnetosphere is generating significant magnetic flux that largely enters the magnetosphere near the Earth's poles. The Maxwell equations indicate that this flux is inducing circuiting Solar Wind Induced Currents (SWICs), as Eqn. 4 indicates both must co-exist. The location of these SWICs within the

magnetosphere is as yet unclear, though intuitively the OC should be considered the prime candidate: a disturbance in the geomagnetic field is communicated to its source (the OC), which then reacts to counter-balance the disturbance. A quick back of the envelope calculation demonstrates that the (outer shell of the) OC is the only plausible SWIC location.

The SWICs generate magnetic counterpressure (Eqn. 5) which Earth surface measurements indicate are roughly one third in size and opposite in direction to the daily geomagnetic variations (Matsushita & Maeda 1965; Baker et al. 1997). Fig. 4 shows a -35 nT contour with a radius of approximately 1000 km, so as a minimum the Earth's reaction (counterpressure) to the on average 5 TW (Dessler 1974; Herman & Goldberg 1978) solar wind disturbance should exceed 12 nT in this area.

The maximum SWIC current I generated by 5 TW in a 1000 km radius circuit can be estimated (Ohm's Law) as:

$$I_{max} = \sqrt{\frac{P_{max}}{R}} = \sqrt{\frac{5.10^{12}\,W}{1/\sigma_{SWIC} * 2 * \pi * 10^6 m}} \approx 892\sqrt{\sigma_{SWIC}}\ (A) \qquad \text{(Eqn. 8)}$$

whereby σ_{SWIC} is the electrical conductivity of the medium through which the current is flowing. The maximum magnetic field strength, B_{max}, in the center of such a circuit can be estimated using the Biot-Savart law (Purcell & Morin 2013):

$$B_{max} = \frac{\mu_{SWIC} * I_{max}}{2r} = \frac{\mu_{SWIC} * 892\sqrt{\sigma_{SWIC}}\ (A)}{2 * 10^6\ m} \approx\ 4.5 *\ 10^{-5} *\ \mu_{SWIC} *\ \sqrt{\sigma_{SWIC}}\ (nT) \qquad \text{(Eqn. 9)}$$

whereby μ_{SWIC} is the magnetic permeability of the SWIC medium.

Material	σ (S/m)	μ (H/m)	B_{max} (nT)
Iron	10^7	6.0E-03	8.5 10^6
Sea Water	10	1.3E-06	2
Ionosphere	10	1.3E-06	2
Igneous	10	1.3E-06	2

Table 1: Order-of-magnitude representative maximum conductivity and magnetic permeability values for selected media found withing Earth's magnetosphere, and maximum magnetic flux density (from Eqn. 9) inducible in a 1000 km radius loop by 5 TW.

Eqn. 9 indicates that the magnetic field strength increases linearly with current intensity: large electric currents flowing in magnetically permeable media generate strong magnetic fields. Eqn. 8 however indicates that for a constant power source a large percentage of the energy of any magnetogenic process is lost as waste heat in materials with low conductivity, and that such power losses increase quadratically as a function of current intensity. Table 1 demonstrates that the Earth's ferromagnetic OC is the only location within the magnetosphere where SWICs can plausibly generate significant magnetic fields. Proposed magnetogenic processes in low magnetic permeability media such as Callisto and Europa's internal salt ocean (Zimmer et al. 2000), Saturn's (Cowley et al. 2004) or Earth's (Daglis et al. 1999) ionosphere, or the Earth's Mantle (Merrill et al. 1998) are therefore very unlikely, as they all would require improbably large power sources (Eqn. 8), and result in the generation of enormous amounts of waste heat that is not in evidence. For example, Eqns. 8 & 9 indicate that for a given magnetic flux density the current intensity of an ionospheric loop would have

to be 4.6 10^3 times stronger than for an iron circuit, and would therefore require a power source and generate waste heat that are 10^{14} larger.

Zimmer et al.'s (2000) approach - comparing the induced fields of Callisto and Europa to a perfectly conducting sphere - is somewhat misleading, as all the supplied magnetic flux energy in such a model is converted to induced magnetic energy with no waste heat losses: in Eqn. 1 both waste heat losses as well as electromagnetic absorption losses are lumped together in the "A" factor. The observations that A ≈ 1 indicates both waste heat losses as well as mantle absorption losses are low, which the authors interpret is due to the shallow depth of the magnetogenic source layer – a hypothetical liquid salt water ocean. The above analysis indicates that magnetogenesis in such a low conductivity layer suffers enormous waste heat losses (A << 1), which were not observed. A more likely model is that Callisto and Europa's magnetic fields are induced in their high conductivity, high magnetic permeability ferromagnetic cores, and that the mantle absorption loss model – the authors' skin depth model – is overestimating electromagnetic energy absorption.

Commonly-accepted skin depth models

The main issue with diurnal solar wind generated magnetic flux (DSWGMF) as a power source (and a unified Galilean magnetogenic physical model) is that a significant amount of energy must pass through a planet or satellite's atmosphere and mantle before it can be absorbed and processed by its ferromagnetic core. Qualitative arguments indicate this is less of a problem than would initially appear:

- The Earth's Mantle must let a significant amount of magnetic energy through, otherwise no geomagnetic energy generated in the OC would be observed at surface.
- At the magnetopause the geomagnetic field is exerting magnetic counterpressure against the solar wind deformation in real-time. The solar wind and the geomagnetic field are in a dynamic pressure balance (Schultz 1991), which can only occur if significant magnetic flux is entering and leaving the OC via the Mantle. As the OC is very likely above its Curie temperature, and therefore very likely has no permanent magnetization, such counterbalancing energy is likely being generated in real-time in the OC, indicating some diurnal geomagnetic flux energy is very likely participating in the flux-to-current-to-counterpressure process: the Earth's magnetosphere is reacting to the incident solar wind in a manner similar to that predicted by Eqn. 1.

The amount of magnetic flux energy lost to the Earth's atmosphere is fairly minor: the daily magnetic variations measured above the ionosphere are very similar to those measured at the Earth's surface (Turner et al. 2007). The quantification of the amount of DSWGMF losses to the Mantle requires the quantification of the frequency dependency of the Mantle's absorption properties. Absorption losses, A', for an EM wave travelling through a shield are commonly estimated using equations of the form (Ott 2009):

$$A' = function(T, \sqrt{\mu_r * \sigma_r * f}) \qquad \text{(Eqn. 10)}$$

whereby T is the thickness of the shield, f the frequency of the wave, and μ_r and σ_r the relative magnetic permeability and electric conductivity resp. of the shield material. Note that Zimmer et al.'s (2000) skin depth model for Callisto and Europa is also of this form.

In general, Eqn. 10 predicts that lower frequency EM waves will suffer less absorption losses than higher frequency waves when travelling through shields. The geomagnetic field is commonly believed to be spawned in the OC (Merrill et al. 1998; Stacey & Davis 2008), so its outgoing magnetic energy likely travels as a low frequency wave through the Mantle: any high-frequency geomagnetic field energy would be shielded by the thick overlying Mantle and would not be observable at surface. Estimates of Mantle absorption therefore often focus on calculating the highest frequency that will not be screened. Previous workers (for example Merrill et al. 1998; Zimmer et al. 2000; Kuvshinov 2008) assume a static conductivity (σ_r) model, constant magnetic permeability (μ_r) and $\partial D/\partial t=0$ to estimate the absorption of EM waves. For example, Merrill et al. 1998, estimate Mantle skin depth **δ**, the depth at which the amplitude of an EM wave has fallen to 1/e of its original value, by assuming a constant value of $\sigma = 1$ S.m^{-1} for the Mantle. The lowest frequency wave period that will not be screened is then estimated - assuming **δ**=2000 km - as approximately half a year (Merrill et al. 1998), indicating that the Mantle acts as a band-pass filter that roughly shields all frequencies greater than 10^{-7} Hz from entering or leaving the OC. A number of observations indicate that this cut-off limit is at least several orders of magnitude too low:

- The magnetosphere size varies in real-time with solar wind pressure (Crooker et al. 1977; Schultz 1991; Stamper et al. 1999; Kivelson & Bagenal 2014), indicating a real-time interaction between the solar wind and the geomagnetic field is taking place, and not one that is delayed by 6 months.
- The geomagnetic field recovers from its daily deformation in 6 hours (Fig. 5) and solar storm events – short, high-energy events similar to the solar wind – in "2-3 days" (Merrill et al. 1998; Kivelson & Bagenal 2014).
- Geomagnetic jerks - a relatively abrupt change in the second derivative of the Earth's magnetic field with respect to time – are generated in the OC, yet globally appear synchronously (Le Mouël et al. 1980).

The frequency dependency of magnetic flux absorption

Eqn. 4 indicates that time-variant geomagnetic flux density ($\partial B/\partial t$) generated by the diurnal geomagnetic field variations caused by the solar wind induces a spatially or temporally varying, circuiting electric field ($\nabla \times E$) that spawns currents. Similarly, a time-variant electric flux as well as an electric current give rise to a circuiting magnetic field. Therefore significant planetary magnetic fields (large magnetic counterpressure) can only be induced in materials with high electrical conductivity (σ) and magnetic permeability (μ). These properties are however frequency-dependent.

Eqn. 10 is an engineering equation that somewhat masks reality. It is the properties of the medium, not the frequency of an EM wave itself, that is important in determining the amount of absorption: for example, in space no absorption of any electromagnetic energy of any frequency occurs because $\sigma_r = 0$. The conductivity and magnetic permeability of all materials changes as a function of EM frequency. Eqn. 10 is therefore more scientifically re-written as:

$$A' = function(T, \sqrt{\mu_r(f) * \sigma_r(f)}) \qquad \text{(Eqn. 11)}$$

The static conductivity model, constant magnetic permeability and $\partial D/\partial t=0$ used in commonly-accepted skin depth models are therefore inappropriate simplifications when determining the Mantle's absorption of EM waves with frequencies below 1 kHZ, as the EM

properties of the Earth layers - μ_r and σ_r –vary greatly with frequency (Schelkunoff 1943; Ott 2009), and $\partial D/\partial t$ is obviously non-zero for an EM wave. The shielding effectiveness of all materials decreases radically below 100 kHz, and both absorption and reflection losses are low for a low-frequency EM pulse (Schelkunoff 1943; Ott 2009). This well-known frequency-dependency has numerous applications, ranging from ground-penetrating planetary radar (Neish & Carter 2014), to EM Sounding of planetary interiors (thousands of km of ground penetration; Banerdt et al. 2014), to submarine and underground mine communication systems (Ott 2009).

For EM waves below 100 kHz the $\sqrt{\mu_r(f) * \sigma_r(f)}$ absorption term in Eqn. 11 decreases rapidly as a function of *f* for non-ferromagnetic materials, such as Mantle silicates, but decreases much less rapidly for ferromagnetic materials as their μ_r increases more than their σ_r decreases (Schelkunoff 1943; Ott 2009). For example, the relative magnetic permeability of steel increases three orders of magnitude between 10 GHz and 100 Hz, while the magnetic permeability of non-ferromagnetic materials remains constant ($\mu_r \approx 1$; Ott 2009). This implies that many commonly-accepted skin depth models (Merrill et al. 1998; Zimmer et al. 2000; Kuvshinov 2008) greatly overestimate Mantle absorption: at low EM frequencies the electric conductivity of all materials drops to values whereby they cannot significantly interact with the electrical field of an EM wave. However, ferromagnetic materials can interact with the magnetic field of a low-frequency EM wave due to their increasing μ_r. EM-sounding applications utilize this frequency dependency: between 1MHz and 1 μHz the Earth's physical response changes from "wavelike" to "inductive", and deep Earth studies use frequencies on the order of 10^{-3} Hz (Banerdt et al. 2014). Therefore:

- High EM frequency band > 1 kHz: the non-ferromagnetic Atmosphere and Mantle potentially absorb significant amounts of EM energy
- Low frequency band < 1 kHz: only the ferromagnetic OC absorbs significant amounts of EM energy

The Merrill et al. (1998) band-pass boundary of 10^{-7} Hz is very likely several orders of magnitude too low: the magnetic flux frequencies of 10^{-5} Hz (Earth) and ~2 x 10^{-5} HZ (Galilean Satellites; periods ~12 hours) very likely lie well within the range of frequencies whose EM wave energy is largely absorbed by their metallic cores.

THE SOLAR-WIND-INDUCED-ELECTROMAGNET PHYSICAL MODEL

The previous chapter demonstrated that a significant amount of DSWGMF passes through a planet's non-ferromagnetic mantle and is absorbed by its ferromagnetic core, and that it is therefore a plausible magnetogenic energy source. Earth's geomagnetic and geothermal data can be used to derive a generic Solar-Wind-Induced-ElectroMagnet (SWIEM) model from the Galilean satellite magnetogenic process.

The Induced Fields of the Galilean Satellites

The Galilean satellites' ferromagnetic cores very likely absorb most of the primary ~2 x 10^{-5} Hz EM wave energy that is generated during their path through the Jovian magnetosphere. Eqn. 4 predicts this core-absorbed time-variant magnetic flux will cause time-variant circuiting currents in their high-conductivity cores, which in turn Eqn. 5 indicates will induce low frequency counterbalancing magnetic flux that passes back through the mantle without

significant attenuation. The whole flux-to-current-to-counterflux process therefore progresses without significant energy loss (Eqn. 1; A ≃ 1): magnetogenic waste heat losses are low.

Ganymede has an intrinsic field that carves out its own mini-magnetosphere within Jupiter's larger one. Its dipole moment is also antiparallel to Jupiter's, and induction signatures are observed (Collins & Johnson 2014), yet its field strength is greater than a reactive induced field: additional power is likely supplied by the magnetic flux of the ambient solar wind "plasma" that flows around the Galilean satellites (Zimmer et al. 2000).

Solar Wind Induced Currents

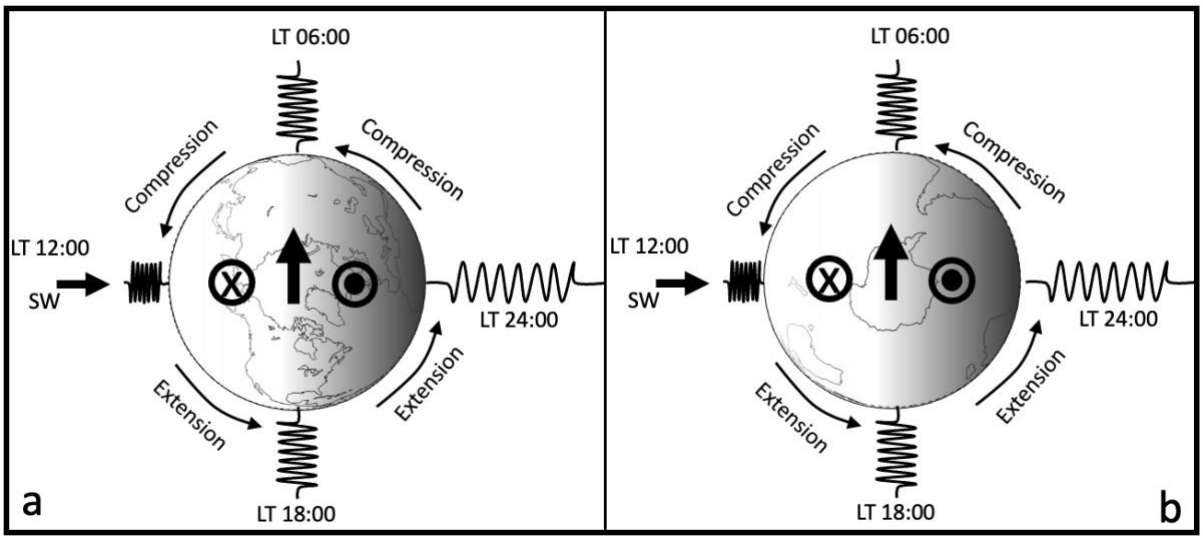

Figure 6: polar-view schematics of how a Solar Wind Induced Current (SWIC; central arrows) is generated. a) northern hemisphere; b) southern hemisphere. Circled X's reflect maximum positive magnetic flux density; dotted circles maximum negative magnetic flux density. Earth continent outlines and coiled springs provided for illustration purposes.

The Galilean satellite data demonstrates that external magnetic flux is inducing currents that power the magnetic fields of the satellites. Similarly, the DSWGMF must be generating a circuiting current that attempts to undo (Eqn. 4) the magnetic deformation caused by the solar wind. At the LT 12:00 position the maximum solar wind pressure is met by the maximum geomagnetic field counterpressure that is induced (Eqn. 5) by a circuiting current (Eqn. 4). The compression of the Earth's magnetosphere is analogous to the traditional grade school experiment whereby one magnet (A) is used to push a same-pole magnet (B) around a table without touching it. The movement of magnet A into the vicinity of magnet B causes the compression of magnet B's and A's fields, which generates magnetic flux that induces currents in the magnets (Eqn. 4) that will attempt to generate a magnetic field that counterbalances/cancels the deformation, thereby creating counter-pressure at the A-B magnetic interface that pushes magnets A and B away from each other and restores their original magnetic fields. Note that for illustration purposes the solar wind induced currents (SWICs) are portrayed two-dimensional loops but that in reality the three-dimensional deformation of the magnetosphere (Fig. 4) induces three-dimensional current sheets whose integrated response effects three-dimensional counterpressure. For example, a 3D SWIC is generating counterpressure in Fig. 4, but for discussion purposes a 2D SWIC circuit generating counterpressure for the -35 nT deformation is considered.

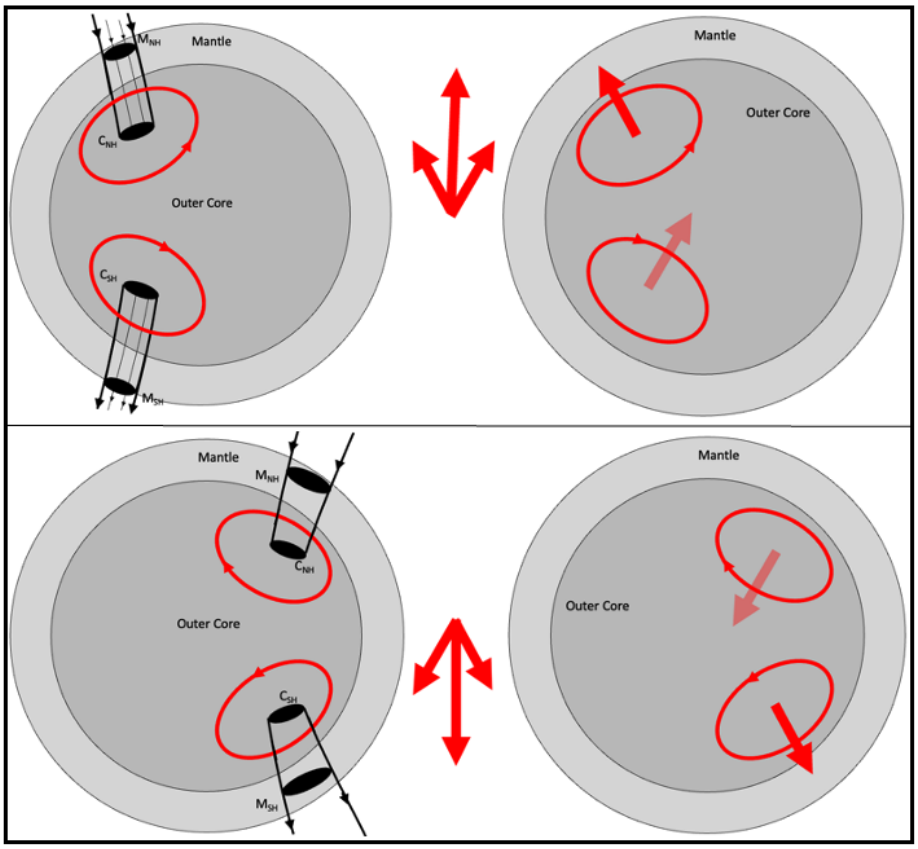

Figure 7: schematic of counterclockwise (as seen from the north) SWIC circuit couples generating a "reverse" polarity magnetic field (top) and clockwise SWIC circuits generating a "normal" polarity field. Black lines are magnetic field lines; black ovals present flux patches(C=Core, M=Mantle, NH=Northern Hemisphere, SH=Southern Hemisphere). Red loops represent solar wind induced current (SWIC) circuits. Thick red arrows represent poloidal magnetic moments. Combined NH and SH SWIC circuit magnetic moments plotted at the geographical equator. Not to scale.

As discussed above, the maximum change in positive magnetic flux density occurs near the high-latitude LT 12:00 "sweet-spot", while the maximum negative magnetic flux density change occurs in a high-latitude LT 24:00 "sweet-spot" (Fig. 6). These areas induce strong Solar Wind Induced Currents (SWICs) that attempt to undo the solar wind deformation by inducing magnetic counterpressure. As the magnetic field lines have a positive inclination in the NH (go into the page in Fig. 6a) the induced magnetic field flows out of the page at the LT 12:00 location, counterbalancing the increase in magnetic flux density, and flows into the page at the LT 24:00 location (Fig. 6a), counterbalancing the decrease in magnetic flux density. The induced current (SWIC) therefore flows towards the LT 06:00 location (right hand rule).

The areas of maximum positive (LT 12:00) and negative (LT 24:00) geomagnetic flux density are determined by the solar wind direction, and are therefore identical in the SH (Fig. 6b). In the SH however the magnetic field flows out of the page in Fig. 6b, so the counterbalancing induced magnetic field flows into the page at the LT 12:00 position, counterbalancing the increase in magnetic flux density, and out of the page at the LT 24:00 position (Fig. 6 b), counterbalancing the decrease in magnetic flux density, thereby also resulting in a SWIC to the LT 06:00 position (right hand rule).

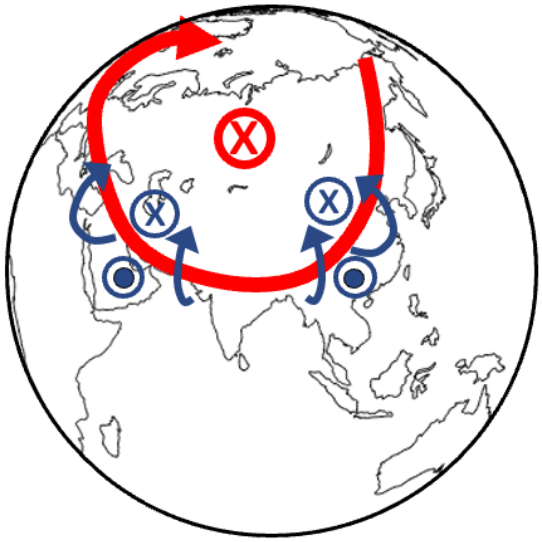

Figure 8: schematic of a SWIC circuit inducing poloidal (red) and toroidal (blue) magnetic fields. Earth continent outline provided for illustration purposes. Circled X's reflect a magnetic moment into the page; dotted circles a magnetic moment out of the page.

The NH and SH SWICs initially flow in the same direction, that is towards the LT 06:00 side of the planet (Fig. 6, 9) along or to the CMB while only incurring limited Ohmic heat energy losses in the high-conductivity core. The mantle beyond the CMB forms a low-conductivity barrier, so the SWIC must bend its trajectory to avoid entering it and continuing its least-resistivity path in the outer shell of the core by following the LT 06:00 meridian towards the magnetic equator (circled X in Fig. 9).

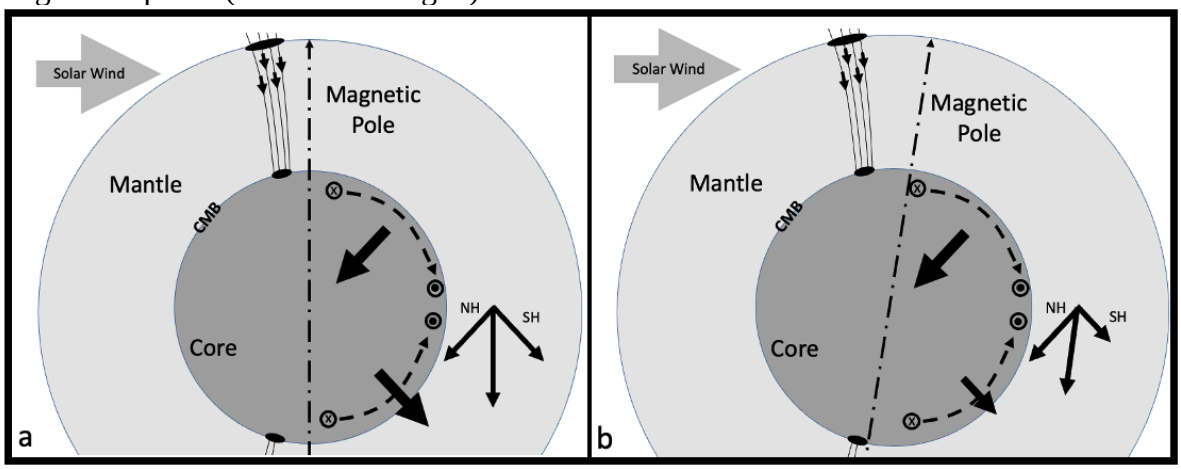

Figure 9: planet cross-section schematic of a SWIC loop generating a "normal" polarity magnetic field. CMB=Core Mantle Boundary. Thin dashed arrows indicate initial (projected) solar wind induced current (SWIC) paths. Circled X's reflect SWIC flow into the page (towards LT 06:00); dotted circles electric circuit flow out of the page (toward LT 18:00). Dot-dash line is the magnetic field dipole axis. Combined NH and SH SWIC circuit magnetic moments plotted at the geographical equator. (a) Equal strength SWICs. (b) relatively strong NH SWIC, weak SH SWIC. Not to scale.

The mutual EM repulsion of the SWICs and the geometry of the solar wind deformation of the magnetosphere (Fig. 4) force each SWIC to circuit back to its point of origin. The simultaneously-spawned NH and SH SWICs therefore must deviate either towards the east (counterclockwise SWICs as seen from the North) or to the west (clockwise SWICs; thin arrows in Fig. 9) before reaching the (magnetic) equator. A clockwise SWIC circuit (Fig. 7 bottom; Fig. 9) generates a (poloidal) magnetic moment in the direction of the Southern

hemisphere ("normal" polarity), that is increase the flux at the LT 24:00 position and counteracts (increases) the LT 24:00 negative flux density caused by the solar wind deformation. A counterclockwise circuit (Fig. 7 top) generates a (poloidal) magnetic moment in the direction of the Northern hemisphere ("reverse" polarity), that is counteracts (decreases) the increase in flux density at the LT 12:00 position. A diverging SWIC (both east and west circuiting currents) would result in a highly-unstable (and therefore unlikely) magnetic field that locally reverses itself every 12 hours. Note (Fig. 8) that SWICs induce both a poloidal (red) and planet-internal toroidal (blue) fields.

The SWIEM physical model: dipole and non-dipole field generation

The following discussions assume an Earth-similar magnetic field geometry (Figs. 6-12), though the principles are applicable to any planet with a high-conductivity high magnetic permeability (solid or fluid) ferromagnetic core and a low-conductivity low magnetic permeability non-ferromagnetic mantle. The clockwise SWIC circuits (as seen from the North) in Figs. 8-13 have a magnetic moment in the direction of the Southern hemisphere, that is contribute to a "normal" polarity dipole similar to Earth's present-day dipole. Two equal-strength SWICs (Fig. 7 bottom, Fig. 9a) generate (poloidal) magnetic moments with contrasting tilts: their sum at the geographic (in this case also magnetic) equator is a dipole field with no tilt (no radial component as their magnetic moment tilts cancel each other out), though in the center of their circuits their tilts cause a large local radial (non-dipole) component in their respective hemispheres.

The total DSWGMF power absorbed by the core, P_{tot}, is partially dissipated as waste heat, P_Q, and partially stored as induced magnetic field energy, P_B.

$$P_{tot} = P_Q + P_B \qquad \text{(Eqn. 12)}$$

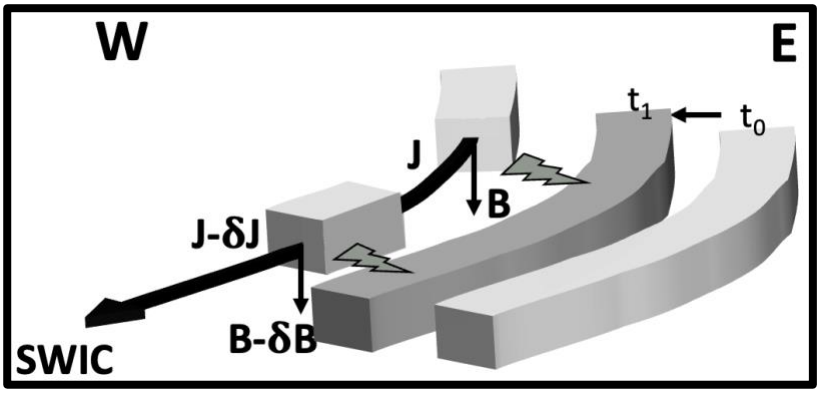

Figure 10: schematic of a "normal" polarity SWIC contained by heat barriers (grey curved beams to the E). Along its pathway the SWIC loses strength (**δ**J) due to Ohmic heat losses resulting in a westwardly / inwardly shift of the SWIC over time (t_0 -> t_1) as well as a loss of induced field strength (**δ**B).

The heating of the circuit pathway increases its resistivity (Schelkunoff 1943; Ott 2009). SWIC directional changes (Fig. 10) and EM interference of neighboring circuits' toroidal fields causes peripheral heating (Figs. 8, 10, 11). Heating losses are especially large where the NH and SH SWIC circuits interact along the equator, and along their Eastern boundaries where their currents are strongest. These higher temperature zones (Fig. 11; grey bands) entrench the SWIC circuit, as they form higher temperature resistivity barriers to future

SWICs, possibly causing them to gradually migrate (westwardly in Fig. 10) to colder, lower resistivity pathways unless the heat is effectively shed to the mantle.

The SWIC loops behave as giant resistor-inductor circuits (RL circuits, Purcell & Morin 2013): a time-variant power source (DSWGMF) induces a time-variant current (SWIC) whose circuit causes the inductor (SWIC circuit) to generate a magnetic field while suffering Ohmic heat losses along its pathway (Fig. 7, 9, 10). The synchronous NH and SH SWIC circuits form a mutual induction pair (Fig. 12). When one circuit moment is weaker than the other, for example due to a weak SH SWIC, the combined magnetic moments result in a tilted magnetic pole (Fig. 13a) as well as a possible negative non-dipole over the weaker complex (Fig. 12 b), whereby the weak circuit steals energy from its stronger paired inductor.

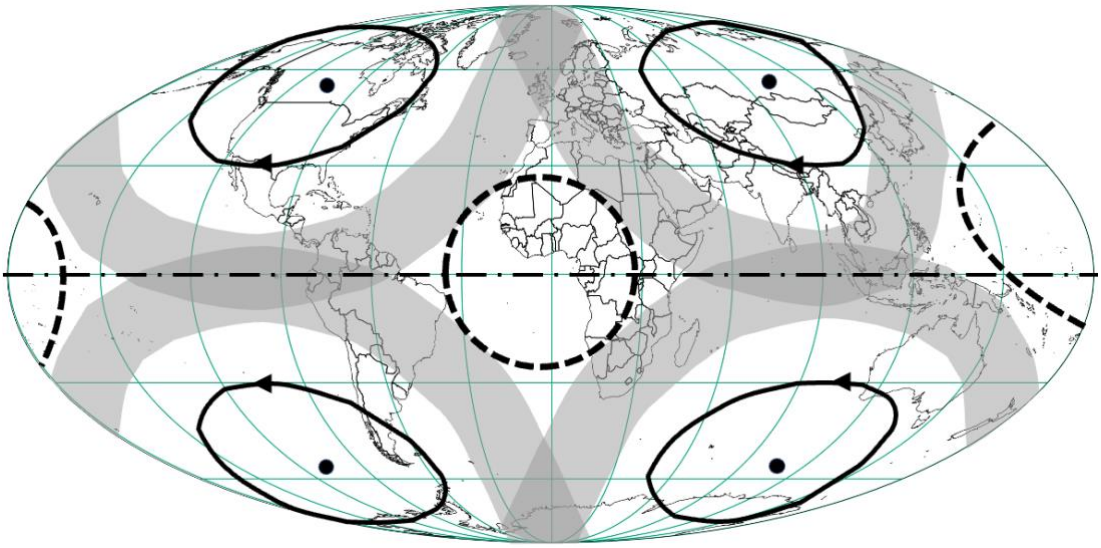

Figure 11: idealized representation of an Earth-similar planet with an axisymmetric dipolar (generated from quadrupolar) magnetic field, with 4 equal-strength SWIC loops (solid black lines; dots represent centers, and therefore non-dipoles) forming 2 pairs of N-S coupled inductors; grey bands are associated heating zones. Dashed lines represent equatorial "thief" SWIC circuits. Equal strength SWIC's. Earth country outlines provided for illustration purposes.

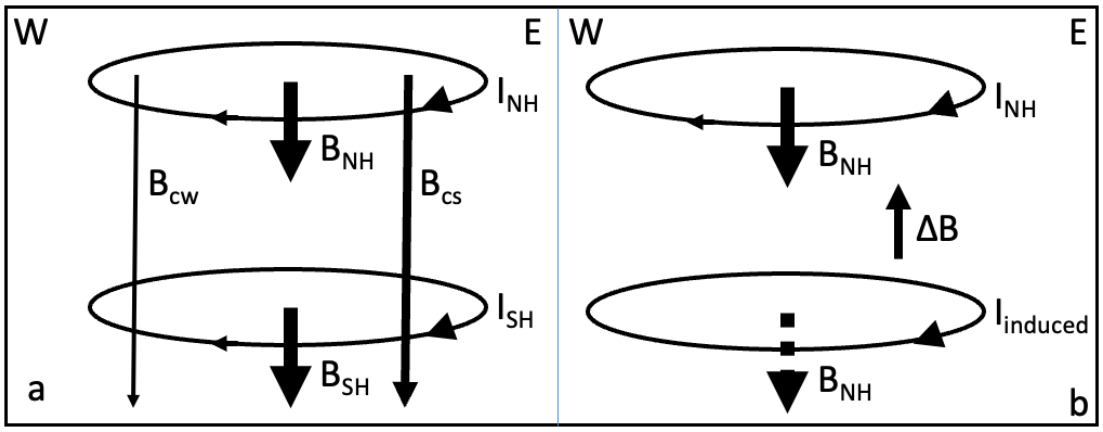

Figure 12: idealized representation of normal-polarity paired NH and SH inductors with non-dipole tilts removed. B: magnetic field; I: current; cs: combined strong; cw: combined weak. a) equal strength SWICs; b) NH SWIC much stronger than SH SWIC resulting in a SH negative non-dipole (ΔB).

The NH-SH paired resistor-inductor SWIC complex geometry displayed in Figs. 11-13 is theoretically very stable, as its boundaries are continually heated (Fig. 10), resulting in roughly steady-state SWIC circuit paths that only change when an accumulation of waste

heat forces a SWIC into a lower resistivity pathway. The magnetic moments of the main SWIC loops (Fig. 9-13) globally combine to form the SWIEM magnetic field, which - when all SWIC complexes are equal strength - globally resembles a dipole, but whose SWIC complex centers form non-dipoles.

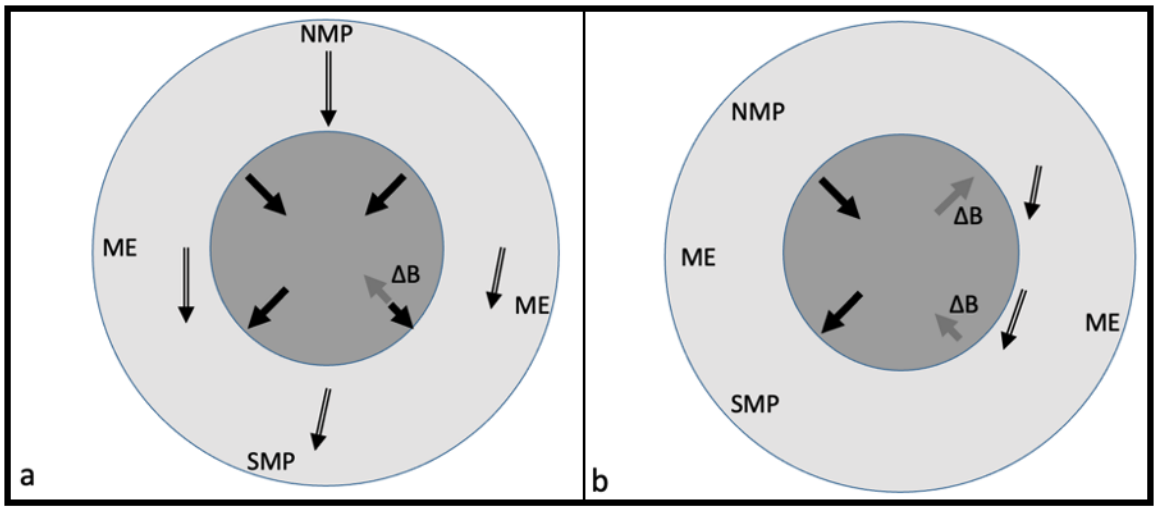

Figure 13: planet cross-section schematic of the magnetic moments of two paired SWIC loops. Solid arrows represent SWIC circuit magnetic moments; double arrows represent combined moments for the geographical poles and the equator. Not to scale. (a) Equal strength SWICs on the left; relatively strong NH SWIC, weak SH SWIC on the right; b) unstable geometry whereby the right-side SWIC's have shut down. MP: magnetic pole; NMP: north magnetic pole; SMP: south magnetic pole; ME: magnetic equator.

The Diurnal Geomagnetic Energy Budget

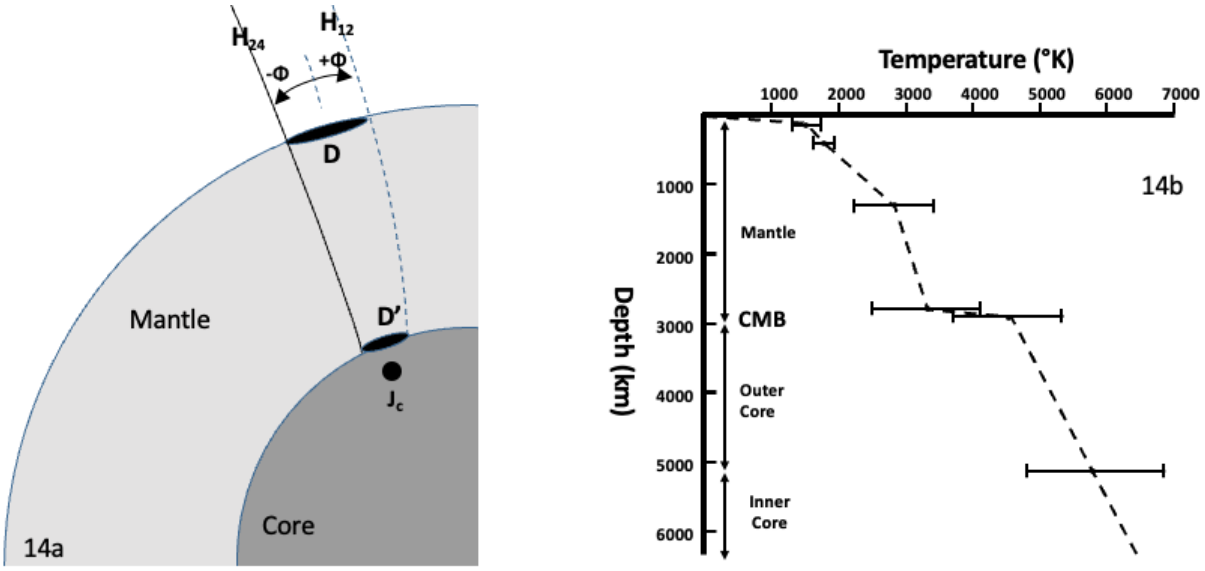

Figure 14: a) Idealized quarter-section through the Earth, showing a geomagnetic field line H during its maximum extension at LT 24:00 (H_{24}; solid line), during maximum compression at LT 12:00 (H_{12}; dashed line), D and D' represent Mantle and OC flux patches resp.; J_C is an electric current induced in the Core; Not to scale. b) geothermal gradient for 14a (dashed line) with the estimated temperature ranges (after Verhoogen 1980)

Both theory and observations indicate that a significant part of the DSWGMF is likely absorbed by the Outer Core (OC). In contrast, an EM wave whose frequency is much greater than 1 kHz will largely be absorbed by the Atmosphere and Mantle: its energy decreases exponentially as it penetrates the Earth until somewhere in the Mantle – at its effective terminus T– it has become so small as to be insignificant. The depth of T is largely dependent on the ability of the Mantle rocks to absorb the pulse's energy, and can be calculated from Eqn. 11 from $\sqrt{\mu_r(f) * \sigma_r(f)}$. Given a constant Mantle composition the depth of T therefore varies as a function of the frequency of the EM wave. The same reasoning does not apply to the DSWGMF, which daily sends a magnetic pulse of roughly constant frequency (10^{-5} Hz) through a roughly identical thickness of Mantle rocks that do not significantly absorb its energy. This low frequency geomagnetic flux enters a flux tube through the Mantle via a flux patch D (Fig. 14a), travels relatively unimpeded through the Mantle due to the Mantle's low σ_r and μ_r at low frequencies, and enters the ferromagnetic OC through a smaller CMB flux patch D' (Fig. 14a), where its energy will start to decrease exponentially as it penetrates deeper into the relatively high μ_r ferromagnetic OC. The largest DSWGMF energy transfer therefore occurs at the CMB (Fig. 14b). A reverse direction reasoning indicates the bulk of the geomagnetic field must be generated in the outer shell of the OC: any low or high frequency magnetic flux generated deep in the Core would be re-absorbed by the outer core shells. The outermost shell of the OC is therefore likely the main location of the geomagnetogenic process.

Significant heating is demonstrably occurring in the outer shell of the OC at the CMB (Fig. 14b), as some heating process must be sustaining the abnormally high 10-12 °C.km^{-1} (Verhoogen 1980) geothermal gradient immediately above it. This heating locally raises the

OC temperature above its adiabatic Core melting curve, resulting in a fluid OC and a lower-than-adiabatic temperature gradient through the Core, which at increased depth and pressure results in a solid (but soft) Inner Core (Tkalčić & Phạm 2018). Once again, observations indicate a strong spatial correlation between heat and geomagnetic field strength: both are collocated in the outer shell of the OC. In this regard it is also highly relevant that the estimated Earth-incident solar wind power of 5 TW (Dessler 1974; Herman & Goldberg 1978) is roughly equal to the estimated total amount of 4 TW of heat lost by the OC to the Mantle (Verhoogen 1980; Merrill et al. 1998), as well as the estimated 3.6-10 TW (Verhoogen 1980) necessary to power the geomagnetic field. Note that this last estimate assumes a (low) dynamo efficiency of 0.1-0.2, but that a magnetogenic process with double that efficiency only requires half the power.

Some diurnal geomagnetic flux must be lost to Mantle absorption during its travel through roughly 2900 km of Mantle rock as its $\sqrt{\mu_r(f) * \sigma_r(f)}$ term is small but non-zero. Observations allow some first-order quantifications. First, consider a flux tube that follows the geomagnetic field lines, and that connects a flux patch at the Earth's Mantle surface, D, to its counterpart on the CMB, D' (Fig. 14a). The magnetic flux that enters the flux tube at the surface will exit the tube at the CMB minus any flux energy absorbed by the Mantle. The time-variant magnetic flux that reaches the OC will induce (Eqn. 4) a time-variant current, which in turn (Eqn. 5) will induce a magnetic field that counterbalances (negative sign in Eqn. 4) the diurnal geomagnetic flux. Assuming the OC flux-to-current-to-counterflux process is 100% energy efficient (no waste heat loss), the magnitude of the daily S_q magnetic flux entering the OC at flux patch D', M, will equal the counterbalancing magnetic flux out. If α is the percentage of magnetic flux M that passes through the Mantle, then the amount of flux entering the flux tube at flux patch D is M/α, and the magnetic flux returning to surface (assuming linear Mantle behavior) is then α*M. Internal Earth-induced magnetic currents are roughly one third in size and opposite in direction to the daily geomagnetic variations (Matsushita & Maeda 1965; Baker et al. 1997), so as a first approximation, at the Earth's surface:

$1/3\ M/\alpha = \alpha * M$ (Eqn. 13)

or α = 58%. This represents a lower limit of the amount of diurnal solar wind generated magnetic flux energy that reaches the Core, as in practice some energy will be lost as waste heat in the OC due to the inefficiency of the flux-to-current-to-counterflux process: the flux energy into the OC equals the flux energy out minus OC heat losses. Note the assumption that the Earth-internal magnetic variations measured at the surface are generated in the OC: Table 1 indicates the low-conductivity, low magnetic permeability Mantle silicates cannot generate significant planet-scale magnetic fields. The Mantle's low EM properties are the main reason a dynamo driven by Mantle thermal convection is physically unrealistic. The OC is the only credible source of significant internally-generated magnetic energy.

Mantle flux absorption is very likely much lower than 42%: Eqn. 13 assumed 100% efficiency of the flux-to-current-to-counterflux energy conversion process, while in practice a significant portion of this energy is lost as waste heat during these conversions. In fact, assuming that the bulk of the diurnal geomagnetic flux is eventually converted to Mantle or OC heat leads to a second estimation approach. Figure 14b shows a fairly constant thermal gradient over most of the Lower Mantle (0.3-0.4 °C.km^{-1}; Verhoogen 1980), as well as over most of the OC, though the two are separated by an extremely high geothermal gradient (10-12 °C.km^{-1}; Verhoogen 1980) through the lowermost Mantle (D") layer. Assuming that this

system is roughly steady-state implies that a relatively constant OC heat source is actively maintaining this abnormally high gradient via the CMB. Assuming the D" layer has the same thermal conductivity as the rest of the lower Mantle, and that all heat transfer occurs via conduction, the ratio of the geothermal gradients is equal to the ratio of the heat flux through the D" enveloping spheres, which in turn is equal to the ratio of power necessary to maintain the gradients (Verhoogen 1980; Merrill et al. 1998) so:

$$\frac{P_{CMB}}{P_{D" surface}} \approx \frac{10-12\,℃}{0.3-0.4\,℃} \qquad \text{(Eqn. 14)}$$

implying that 96-98% of the solar wind energy is absorbed by the OC. This is likely an overestimation, as it assumes all heat transfer occurs via conduction.

Third approach: an estimated 4 TW (Verhoogen 1980; Merrill et al. 1998) of heat power is lost by the Core to the Mantle via the CMB. Assuming this amount equals the power reaching the OC yields:

$$\alpha = \frac{4\,TW}{5\,TW} \qquad \text{(Eqn. 15)}$$

or $\alpha \approx 80\%$. This α will serve as a fit-for-purpose, conservative approximation. Note that an OC solar wind power absorption of 4.0 TW (5 TW * 0.8) fits well with the estimated 3.6-10 TW necessary to power a steady-state geomagnetic field (Verhoogen 1980).

Time-variable Diurnal Geomagnetic Variability

The previous sections dealt with the solar quiet (S_q) diurnal variations that are caused by the roughly steady-state solar wind emitted from the Sun's corona, that is the "time-constant", "static" solar wind energy absorbed by the magnetosphere, which can be seen as the main energy source powering the steady-state geomagnetic field. Additional time-variable "dynamic" solar wind energy, termed solar daily disturbance energy (Merrill et al. 1998), S_D, is measured by the aa index. The name of the index is derived from the two (or more) antipodal stations whose measurements are used in its calculation: using antipodal stations reduces local variability effects due to for example latitude and season differences (Mayaud 1972). The aa index has been calculated since 1868 from locally-measured K indices (values 0 - 9) that describe the extra amount of geomagnetic field variability (the S_q signal is first removed) over a three-hour interval. The resultant 3-hourly time series shows a significant correlation with the 11-year solar cycles (Mayaud 1972; Herman & Goldberg 1978), as well as sunspot counts (Mayaud 1972; Dessler 1974; Crooker et al. 1977; Herman & Goldberg 1978; NOAA 2021). The index is therefore a measure of the time-variable solar wind strength, and should be considered as an additional, time-variant energy source.

The historical aa index data were downloaded from the ISGI server [dataset]. To keep calculations simple, a unit volume sphere V_u with radius 0.564 m (cross-sectional area = 1 m^2) is employed. The magnitude of S_D acting on V_u equals the aa index, but its direction is variable. However, any geomagnetic field variation will encounter a V_u cross-section of 1 m^2, irrespective of direction: a magnetic flux density variation of 1 nT therefore always results in a magnetic flux of 1 nWb within V_u. The total change in S_D magnetic flux for (e.g.) 2019 in V_u can then be approximated as the sum of the absolute difference of all the 2019 serially-

adjacent aa index values, and the total 2019 induced electromotive force (Eqn. 4) in V_u can be estimated as:

$$F_{E\_2019} = \int_{2019} \frac{\delta B}{\delta t} \approx \sum_{2019} \Delta aa \quad \text{(Eqn. 16)}$$

$$\Delta aa = |aa_t - aa_{t-3h}| \quad \text{(Eqn. 17)}$$

whereby Δaa represents the absolute difference between an aa index measurement and the one measured three hours earlier. Note that the absolute value is used as either a negative or positive magnetic flux results in a positive energy transfer. For example, the 9 aa index values for January 1, 2019, between 00:00 and 24:00, are 12, 12, 24, 20, 16, 5, 2, 12 and 5 nT respectively. The magnetic flux in V_u is therefore 0+12+4+4+11+3+10+7 = 51 nWb, which according to the Eqn. 4 induces an electromotive force of 51 nV.

Using Eqns. 16 & 17, the total induced 2019 electromotive force in V_u is calculated from the ISGI data as 17.2 μV. If V_u consists of OC material (OC resistivity $\rho \approx 2 \times 10^{-6}$ Ω.m; Merrill et al. 1998) and the energy is fully converted to heat, the estimated induced 2019 Ohmic heating, Q_{aa_2019}, of V_u is:

$$Q_{aa\_2019} = \frac{\varepsilon^2{}_{2019}}{\rho} = \frac{(17.2\ 10^{-6}\ V)^2}{0.564\ m * 2.0\ 10^{-6}\ \Omega.m * 1.m^{-2}} \approx 2.6 * 10^{-4}\ W = 260\ \mu W \quad \text{(Eqn. 18)}$$

To calculate the full power of the S_D time-variant magnetic flux requires summing over all the OC unit volumes that experience it plus catering for Mantle absorption, which is a non-trivial exercise. For this high-level analysis a shortcut is therefore employed. The calculated 1868-2020 average Δaa value is about 10 nT, which should be seen as the average time-dependent magnetic flux that forms part of the average 5 TW (Dessler 1974; Herman & Goldberg 1978) of Earth-incident solar wind power: the estimate uses average solar wind parameters such as average velocity and average density that do not make the distinction between S_q and S_D. Assuming an average $S_q \approx 20$ nT (Crooker et al. 1977), the average S_D represents approximately 33% of their combined total: the 5 TW of average incident solar wind energy therefore roughly consists of 1.7 TW S_D (P_{SD}) and 3.3 TW S_q power (P_{Sq}). Note that only Δaa is time-variant in these calculations, and all other variables are scalars in a steady-state system. Eqn. 16 can therefore be used as a proxy for the time-variant S_D energy (note that 1.7 TW is rounded up to 2 TW for simplicity):

$$P'_{year} = Scalar_1 * \varepsilon^2{}_{2019} = Scalar_2 * (\sum_{year} \Delta aa)^2 \quad \text{(Eqn. 19)}$$

$$\overline{P_{S_D}} = \frac{\sum P'_{year}}{N\ years} = 1.7\ TW \quad \text{(Eqn. 20)}$$

$$P_{year} = \frac{P'_{year}}{2.0\ TW} \quad \text{(Eqn. 21)}$$

The ISGI data are used to calculate $\sum_{year} \Delta aa$, which represents a quantitative measure of the relative power of S_D for a particular year. These yearly sums are normalized to an average of 2 TW (1.7 TW rounded upwards), which avoids the need to worry about scalars while retaining the relative strength of the yearly S_D signal. A graph of this relative power is instructive when testing whether solar wind energy variability correlates with secular

geomagnetic field variability: for example, most globally-observed geomagnetic jerks coincide with P_{year} lows (Fig. 15).

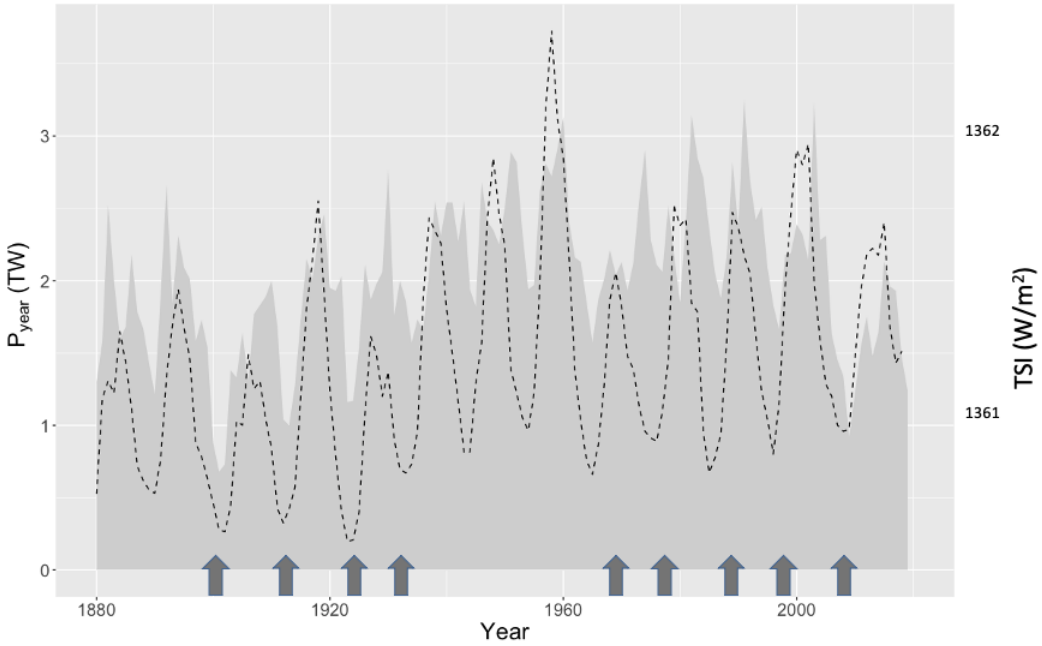

Figure 15: Yearly estimated time-variant S_D solar wind induced power (P_{year}; shaded graph) for the 1880-2020 period, normalized to a 2 TW average; yearly average Total Solar Irradiance (TSI, dashed line) [[dataset] Kopp, G. 2019]; arrows indicate the timing of strong geomagnetic jerks

The geo-SWIEM: Earth's dipolar and non-dipolar fields

The SWIEM model specifies that SWIC circuits can be identified by their non-dipole anomalies in their centers, as well as their peripheral heat anomalies. These characteristics can be used to identify Earth's main SWIC circuit complexes. Figs. 16 a & b represent a 1995 "snap-shot" image of the continuously changing non-dipolar, radial field, B_r. When averaged over the 1690-1990 time period (Fig. 1, top; also compare to Fig. 11), 4 of the main Earth SWIC complexes become apparent due to the persistent relative strength of their non-dipole fields over time: Asia, Australia, North America and South America (Fig. 16 a & b). The Asia-Australia and North America-South America circuits are clearly in paired inductance (Fig. 12): these NH-SH pairs can only jointly increase or decrease in strength.

The last main Earth SWIC circuit only becomes apparent from the 1900-2020 rate of change map (Fig. 16c), which demonstrates a small SWIC circuit near Madagascar is paired to the western part of the Asian circuit. Fig. 16 c indicates that over the last 120 years the North America-South America pair has been jointly decreasing in strength, causing an increasing negative non-dipole over South America, while the Asia-Madagascar pair has been jointly increasing in strength. Note that the center of Madagascar loop appears to be roughly at 30°S, likely due to the higher latitudes of its northern paired loop. The interaction between the American paired inductor loops is evident in time-series animations of the total geomagnetic field strength between 1900-2020 (https://geomag.colorado.edu/main-magnetic-field; accessed: 2022 June 13): the North American total field strength reduces concurrently with the field strength of the South American SWIC circuit (Fig. 13c) as well as the South Atlantic Negative Anomaly (SANA), Earth's largest negative non-dipole which in 2020 is dominated by the weak South American inductor loop.

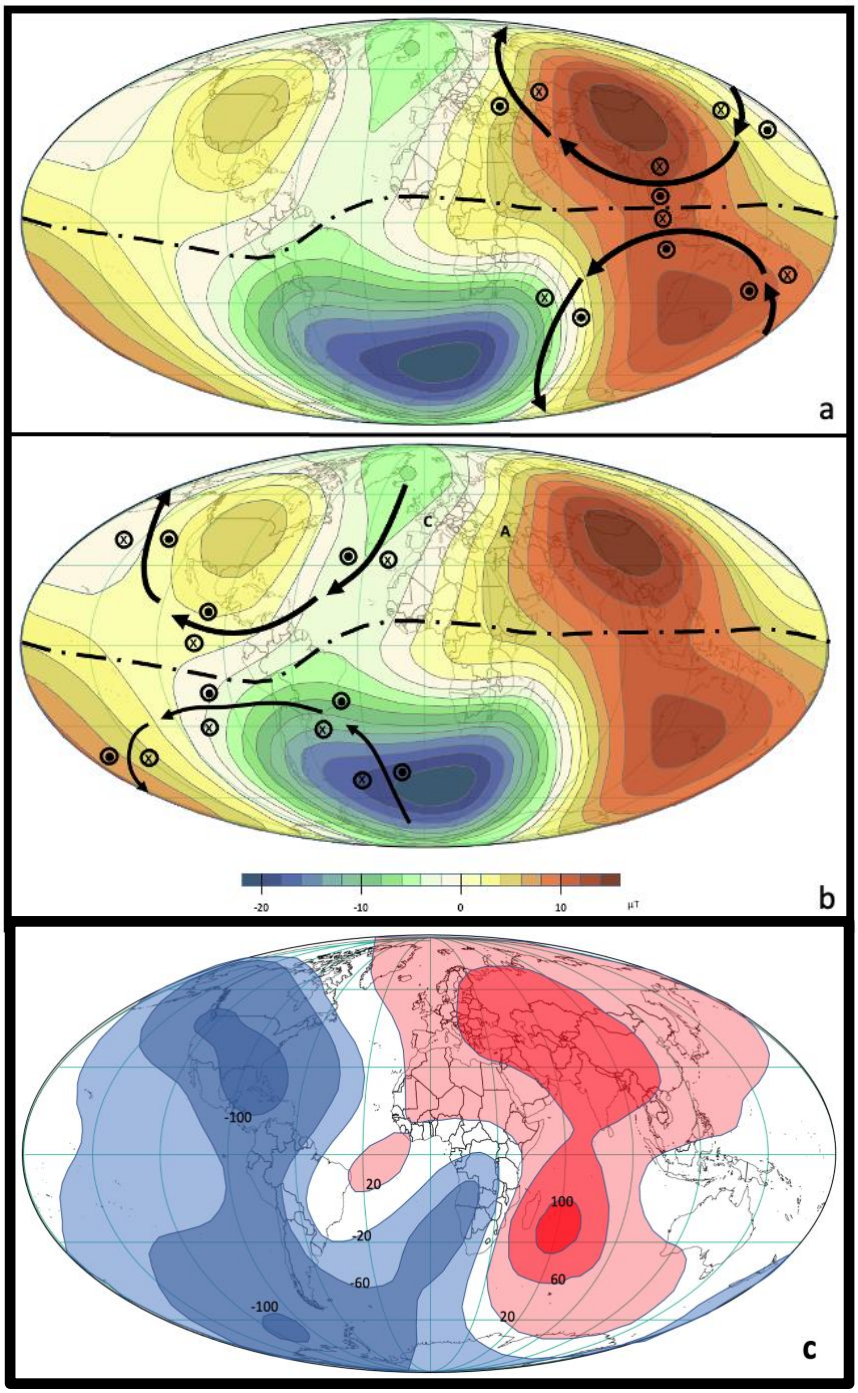

Figure 16: 1995 non-dipolar field strength [after Lühr 2000]. Arrows are conceptual SWIC circuits (projected onto a geographical surface map) for LT 12:00 at 90° W (a) and 90° E (b). Dot-dash line: magnetic equator. Circled X's: induced field into the page; dotted circles: induced field out of the page; (c) Annual rate of change of IRF Total Geomagnetic Field Intensity between 1900-2020 (numbers are change in nT/a; After BGS 2022)

The weakening of the American SWIC pair results in the reduction of their summed NH and SH moments and therefore a decline in their dipole contribution (Figs. 12b, 13a): between 1900 and 1990 the Earth's dipole moment reduced from 8.29 to 7.84 10^{22} Am^2 ([dataset]* Deutsches Geoforschungszentrum (GFZ) 2021), which seems largely attributable to the American paired inductor loops, as the strength of the Asia-Australia pair has remained relatively constant and the strength of the Asia-Madagascar pair has increased. Also note that in 1900 a strong North American SWIC circuit and a somewhat weaker Asian circuit resulted

in a North Magnetic Pole (NMP) that was tilted towards the Americas, but that the continued weakening of the North American SWIC and strengthening of the Asian SWIC is at present likely causing a geomagnetic excursion whereby the NMP will migrate to Asia. Recent data ([dataset] NOAA 2021) suggest that the NMP is currently moving NNW at a speed of 55 $km.a^{-1}$. In 1900 its position (96° W, 70° N) lay near the North American non-dipole center, but in 2020 its current trajectory puts it on-path to the Asian non-dipole center.

Also note the presence of the two coupled equatorial "thief" circuits in the Pacific and North Africa (Fig. 1, top: compare Fig. 11). These weak paired circuits likely periodically "steal" magnetic energy from the other SWIC complexes (Fig. 1, top), resulting in the elongated radial field strength protrusions from the 5 complexes towards the thief loops: if much energy is stolen then the thief loop creates a relatively strong non-dipole over the equatorial loops, while an intermediate (between main SWIC complex and thief loop) non-dipole is generated while when less magnetic energy is stolen.

The geo-SWIEM: heat anomalies

Geothermal heat generation is intimately linked to magnetogenesis: magnetic energy cannot be generated without waste heat losses. Heat maps (Fig. 1 middle; Fig. 17) therefore provide important clues to the processes responsible for generating the geomagnetic field, though they are invariably more difficult to interpret than geomagnetic data as Mantle convection has a large vertical and lateral impact on heat transmission between Core and Crust (Verhoogen 1980; Ekström & Dziewonski, 1998; Merrill et al. 1998; Stacey & Davis 2008). Most surface-observed areas of high heat flow likely originate in the OC (Steinberger 2000; Burke 2011), so magnetogenic waste heat is a likely originator of at least some surface heat anomalies.

In general, the conductive heat flow map (Fig 1 middle) shows a great similarity to the "heating zones" of the idealized SWIC complex map in Fig. 11. For example, the mid-Atlantic ridge roughly follows the geomagnetic non-dipole "saddle" that runs at 90° longitudinal separation from the SWIC complex centers (Fig. 1 middle & bottom), suggesting a causal link between their origins: the mid-Atlantic ridge trajectory follows the areas of high heating (Fig. 11, grey bands) that separate the SWIC complexes. Similarly, the velocity anomalies from Ekström & Dziewonski's 1998 seismic tomography model (Fig. 16 top; correlated to heat) clearly outline the NH (North America, Asia), SH (South America, Madagascar, Australia) SWIC complexes, and the equatorial (North Africa, mid-Pacific) thief circuits. Note that the apex of the North Pacific heating zone is reached at 180° E/W (~90° longitudinal displacement from the Asian and North American SWIC circuit centers), near Wrangel Island (~70° N)

The mid-Atlantic ridge trajectory match (Figs. 1 middle & bottom, 11, 17) is very good for the NH circuit heat and non-dipole data, but is eastwardly displaced by roughly 2000 km south of the equator. This shift is also apparent in Ekström and Dziewonski's 1998 seismic tomography model (Fig. 17 top): the Australian and South American SWIC circuits appear to be eastwardly shifted by 2000 km relative to their inferred locations from the averaged B_r map (Fig. 1 top), though the Madagascar circuit shows a westward shift by a similar amount. The same shifts are also apparent when comparing the heat anomalies (Fig. 1 middle): all heat maps show a South American heat anomaly that seems 2000 km displaced from its radial energy location (Fig. 1 top).

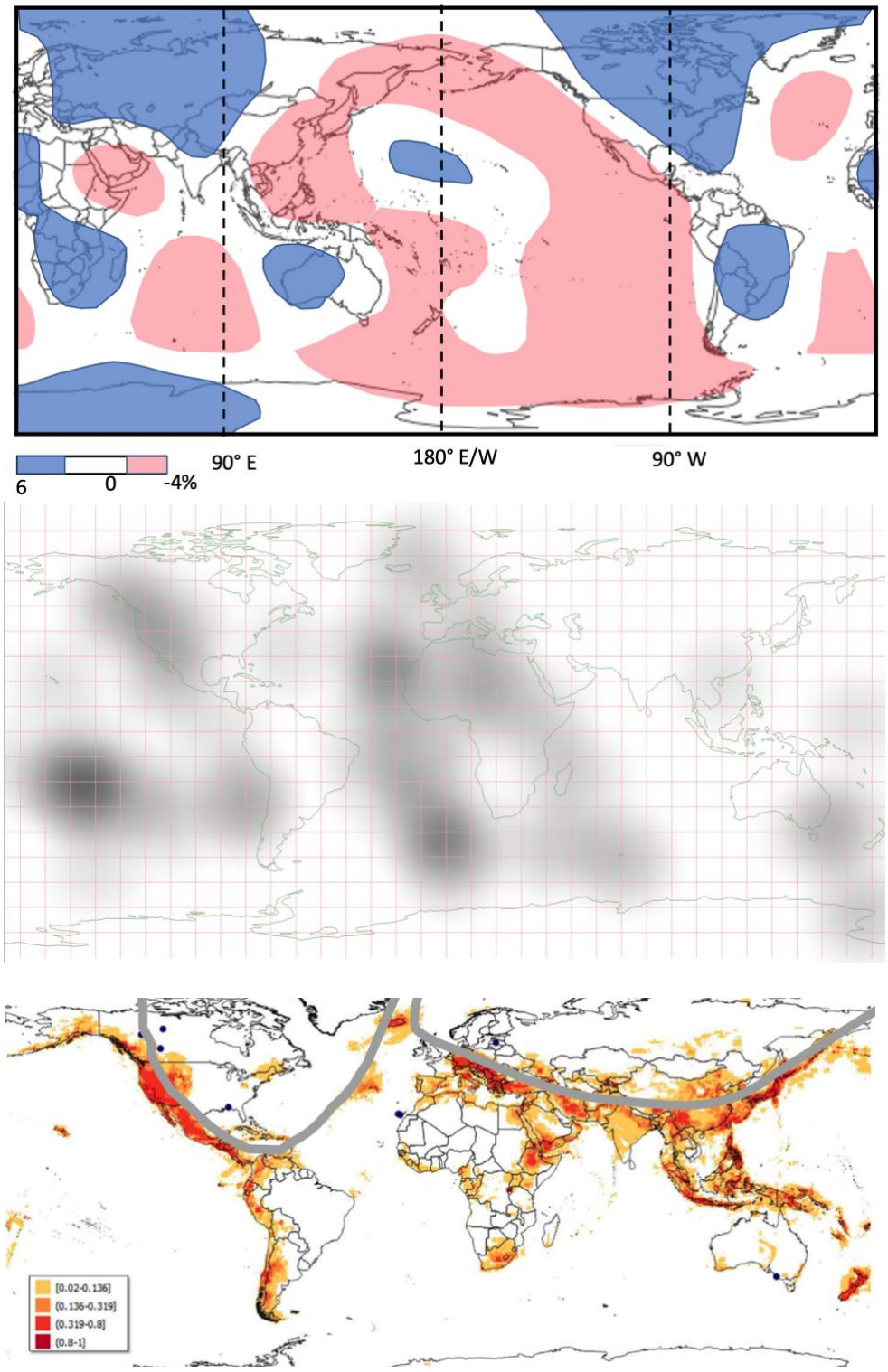

Figure 17:(top) 100 km deep seismic velocity anomalies from a global mantle seismic tomography (after: Ekström & Dziewonski 1998); (middle) Heatmap of recognized hotspots (hotspot density per unit area). Source: [dataset] Morgan and Morgan 2021 Note a 30° (lat/long) search radius was used, leading to more elliptical search areas for the higher latitudes; (bottom) Schematic of northern hemisphere Solar Wind Induction Current loops (grey lines) on a World Geothermal Potential Map (Map Source: http://stellaeenergy.com/energy-transition-16-geothermal-energy)

Note that Ekström and Dziewonski's 1998 study mainly focused on Mantle convection paths, not CMB heat anomalies, and that the seismic wave amplitude attenuation below 250 km depth causes deeper results to be progressively more uncertain. Also note that a 2000 km eastward/westward displacement of the SH SWIC loops does not significantly impact the previous analysis: the NH and SH loops still form mutual inductor pairs.

The mid-Atlantic ridge (and other heat anomalies) are likely acting as long-term resistivity barriers that persist through time, independent of SWIC strength or geomagnetic geometry. The longevity of the mid-Atlantic ridge and many hotspots indicates they likely play a role in steering SWICs during the setup of the dipole/non-dipole geometry after magnetic reversals, in a manner similar to paleogeography steering the course of a new river. Their interactions with the SWIC complexes likely form a very stable feedback loop: the SWICs heat the peripheries of their complexes, regardless of SWIC flow direction, while the higher temperature of the peripheries acts as a resistivity barrier to the SWIC.

An analysis of a hotspot heatmap (Fig. 17 middle; source: [dataset] Morgan & Morgan, 2021) demonstrates that the geo-SWIEM model can rationalize their geographical distribution as well: a large number of hotspots are preferentially formed at the SWIC circuit peripheries, especially on the weaker SWIC side. For example, Fig. 16b demonstrates that the toroidal fields of the American NH and SH SWIC circuits induce contrasting magnetic fluxes on either side of the magnetic equator, which induces an eastward equatorial induction current (right hand rule) to the southern (weaker) side of the magnetic equator, resulting in an Ohmic heating to the south of the equator that is likely responsible for many of the local hotspots.

Both surface heat flow and hotspot density are lowest near the centers of the 5 main SWIC complexes and the North Africa and mid-Pacific thief loops (Figs. 1, 17): areas remote from the SWIC peripheries display negative surface heat flow anomalies. Note that the data sets are often inconsistent as a result of nomenclature: for example, few hotspots have been recognized along the east side of the Asian SWIC complex, that is on the Asian-Pacific plate margin (Fig. 17 bottom), though the high heat flow (Fig. 1) indicates significant SWIC-derived heating.

Global decennial secular variability

Secular geomagnetic variability is likely due to variations in the magnetogenic power source, that is due to the time-variant solar wind energy, S_D. A plot (Fig. 15) of temporal S_D variability versus Total Solar Irradiance (TSI; the amount of solar radiation incident on Earth) confirms their covariance during the last 140 years, and that both co-vary - as expected - with the 11-year solar (sunspot) cycles: good correlations exists between variations in solar wind strength and sunspot counts, and each can be used as a proxy for time-variant solar energy (Dessler 1974; Herman & Goldberg 1978; Eddy 1976).

One much-studied type of secular geomagnetic variability is the geomagnetic jerk (De Michelis et al. 2005; Aubert & Finlay 2019; Aubert 2020). The term "jerk" is borrowed from the field of Electrodynamism and refers to a relatively quick change in the second derivative of the Earth's magnetic field with respect to time. Geomagnetic jerks occur on average every 10 years, a number that is similar to the length of the 10-11 solar cycles, suggesting a link between the two (De Michelis et al. 2005). Strong geomagnetic jerks were observed in 1901, 1913, 1925, 1932, 1969, 1978, 1991, 1999, and 2007 (De Michelis et al. 2005; Aubert & Finlay 2019; Aubert 2020). Fig. 15 demonstrates that nearly all of the strong geomagnetic

jerks occur near P_{year} (S_D) minima (arrows; 1969 is the main exception), indicating the sudden reduction in time-variant solar wind energy, and resultant SWIC strength, is likely causing the jerks.

The time derivative of the Lenz-Faraday equation (Eqn. 4) demonstrates that relatively large and abrupt changes in an induced electromotive force can result in a large change in the second derivative of the geomagnetic field:

$$\frac{\delta F_E}{\delta t} = -\frac{\delta \mathrm{B}}{\delta t^2} \qquad \text{(Eqn. 22)}$$

An induced magnetic field opposes the magnetic flux that created it (Eqn. 4), so a large or sudden change in the induced electromotive force trend will result in a sudden magnetic field adjustment in an opposite trend direction (jerk). During most solar cycles an ever-increasing P_{year} trend abruptly drops off when the Sun reverses its polarity (Fig. 15; Gosling 2014). The trend of the solar wind induced electromotive force hereby abruptly switches from increasing to decreasing near cycle lows, resulting in a sudden reduction in SWIC strength, thereby reversing previously-established induced magnetic field trends and effecting jerks. Note that solar cycle maxima show a much poorer correlation with maximum sunspot counts (and maximum solar wind energy; Mayaud 1972), so strong geomagnetic jerks are less likely to occur at the (more numerous) small-scale trend reversals associated with the more numerous local solar maxima.

Global centennial secular variability

Four major solar minima - Oort, Wolf, Spörer and Maunder - have likely occurred during the last 1000 years (Fig. 18; Eddy 1976; Wu et al. 2018). These periods concur with severely reduced S_D activity (Eddy 1976; Herman & Goldberg 1978), so represent prolonged periods of lower DSWGMF and lower OC energy. Note that Constable et al. (2016; data underlying Fig. 18) focused their efforts on the Southern Hemisphere, so their data may not be globally representative, though in the present high-level context this is largely irrelevant: the time-variant dipole moments measured in SH archeological artifacts, volcanics, and sediments concur with time-variant solar energy (S_D) variations. The covariance of two independent datasets (Fig. 18) indicates that for a large area of the Earth the observed geomagnetic dipole strength variations were likely caused by solar energy variations. Eqn. 12 indicates that a reduction in S_D power effects either a reduction of generated heat energy or generated magnetic energy, or both. The first option is confirmed by Fig. 18: over the last 1000 years all periods of significant geomagnetic dipole moment growth concur with major solar minima, so therefore concur with a reduction in OC heat generation.

The thermal dynamo model predicts that when the Core cools it converts heat energy into magnetic energy (Verhoogen 1980; Stacey & Davis 2008; Aubert & Finlay 2019), that is an increase in magnetic energy and a reduction of heat. The geo-SWIEM model predicts something similar. As mentioned above, between 1900 and 1990 the Earth's dipole moment was observed to reduce from 8.29 to 7.84 10^{22} Am^2, which is a continuation of a centennial trend that started around or possibly before 1100 (Fig. 18). Assuming the last century was a relatively "normal" period leads to the conclusion that the 5 TW of "average" solar wind power (3.3 TW S_q, 1.7 TW S_D) results in an ever-decreasing geomagnetic field strength: this average power is therefore likely mainly (>50%) allocated (Eqn. 12) to increasing OC heat, which results in a higher resistivity along the SWIC paths and therefore a lower SWIC

intensity and a lower geomagnetic field strength. During the four solar minima the S_D energy was largely absent, so the total Earth-incident solar wind power was likely on the order of 3.3 TW, and the OC power on the order of 2.6 TW (0.8*3.3 TW). This effectively meant that the total power supplied to the OC was insufficient to replenish the 4 TW (Verhoogen 1980) of heat lost to the Mantle via the Core-Mantle Boundary (CMB): the OC was cooling during solar minima periods. This cooling resulted in a decrease in resistivity along the SWIC paths and therefore an increase in geomagnetic field strength (Fig. 18).

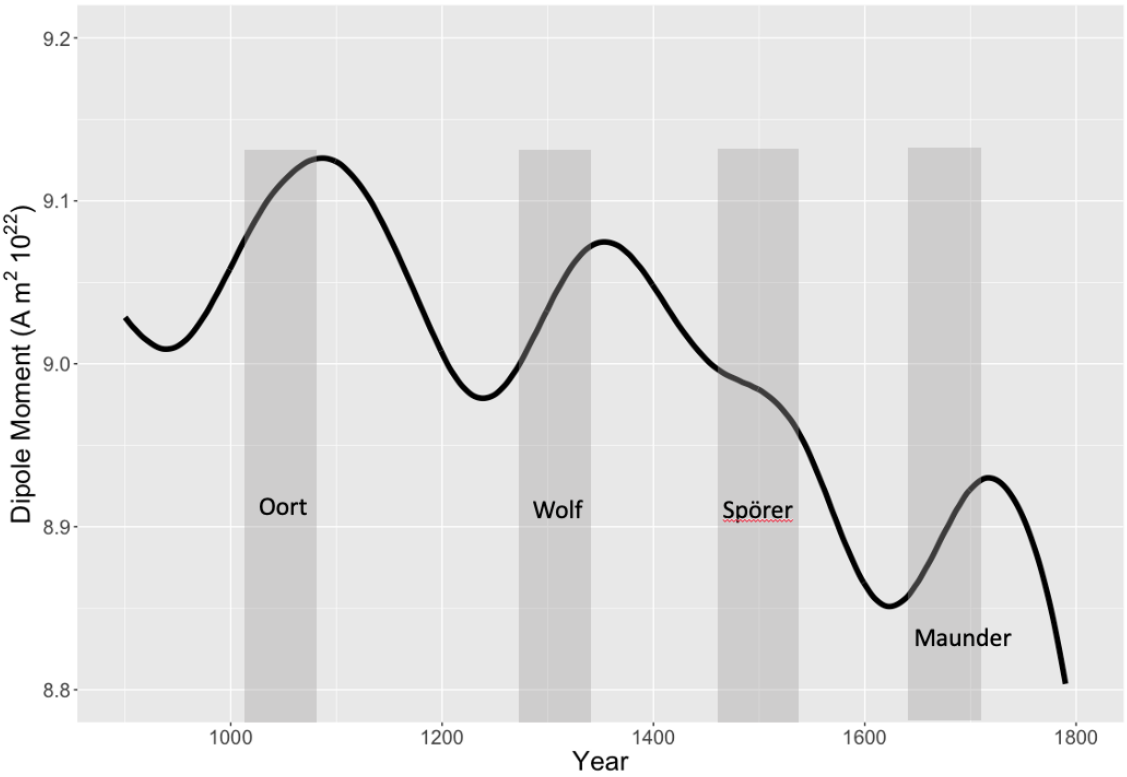

Figure 18: Historical Geomagnetic Dipole Moment ([dataset] Deutsches Geoforschungszentrum 2021) overlain by estimated solar minima periods (shaded columns; Source: Eddy 1976; Wu et al. 2018)

The data allow a rough quantification of the amount of power that the SWIEM allocates to heat generation and magnetic energy (Eqn. 12). During the Oort minimum the magnetic strength increased over 150 years, only to lose these gains over the next 100 years, when the Sun switched its S_D energy back on. Similarly, during the Maunder minimum the gains of 90 years were lost again over the next 50. Both increases and decreases occur in fairly linear fashion: the data are therefore roughly consistent with an allocation of 1/3 to the magnetogenic process and 2/3 to the heating process. Note that a 0.33 efficiency fits well with the measured internal Earth-induced magnetic currents that are roughly one third in size and opposite in direction to the daily geomagnetic variations (Matsushita & Maeda 1965; Baker et al. 1997).

The Geomagnetic Power Spectrum

Numerous authors (for example Banks 1969; Currie 1973) have recognized solar-related line spectra in the geomagnetic power spectrum: the 21.4 year cycle (2 solar reversals; Currie 1973), the yearly and twice yearly cycles (Banks 1969), the 27 day cycle (related to the solar rotation period; Banks 1969), and the daily cycle all show significant power spectrum peaks

that occur on a worldwide scale, indicating they likely represent the Earth's magnetic response to incident solar wind strength variations. These authors attempt to correlate the geomagnetic signal to Mantle conductivity via a model-based inversion process whereby apparent conductivity is converted to true conductivity by assigning the highest frequency measurements to the uppermost Mantle layer via a skin depth model, and iteratively refining the model downwards until it agrees with the observations. The geo-SWIEM model suggests something far simpler: the induction response of the OC is causing the lower frequency internal response observed in the geomagnetic spectrum.

Banks (1969) theorized that the ratio of the external to internal parts of the geomagnetic field at the Earth's surface is dependent on both the external energy source as well as Earth's magnetic response, and determined that a P_1^0 spherical harmonic is an adequate representation of the latitude dependency of the geomagnetic field at the Earth's surface for solar cycles between 0.5 cycles/day and 2 cycles/year. The twice-yearly signal has a frequency of 10^{-7} Hz, which is a deep-Earth response even under Banks' or Merrill et al.'s (1998) likely overly conservative skin depth models. These spectra lines are therefore likely caused by the OC's induction response to the diurnal geomagnetic flux generated by the solar wind. The P_1^0 spherical harmonic is the simplest sectoral harmonic, and signifies that for these low frequency solar cycles Earth's internal response is latitude-invariant. This is entirely consistent with the geo-SWIEM model, as the longitudinal position of the Sun at LT 12:00 determines SWIC strength and direction, not the latitude, so a sectoral harmonic Earth response is both expected and observed. The fact that all cycles between 0.5 cycles/day and 2 cycles/year show a similar response indicates that all the higher-frequency cycles between 10^{-7} and 10^{-5} Hz are likely due the OC's induction response to the DSWGMF. The longer cycles, for example the 27-day cycle, can be seen as multiples of the daily 10^{-5} Hz cycle.

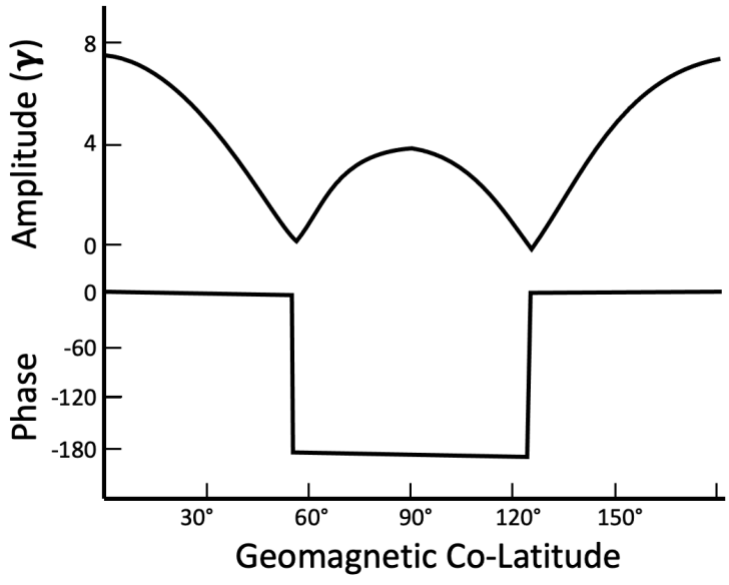

Figure 19: Latitude dependence of the annual vertical (radial) field variation: best least squares fit of Banks' (1969) P_0^2 model

Banks' (1969) study also determined that the annual power spectrum line was better modelled by a P_2^0 spherical harmonic, a tesseral harmonic that is entirely consistent with the yearly response of the geo-SWIEM model. Figure 19 presents the latitude dependency of the vertical (radial) component of Banks' (1969) P_2^0 model, and demonstrates the similarity of

Earth's geomagnetic response for the high latitudes (55-90°N/S), which is very likely due to the shifting of the NH and SH polar sweet-spot locations with the seasons. The Tropic of Cancer (~23° N)/ Capricorn (~23° S) are the most northern / southern circles of latitude at which the sun is directly overhead at the June / December solstice resp. When the Sun is directly over the Tropic of Cancer the SH polar area – and therefore the SH sweet-spot – will have shifted almost entirely to the magnetotail side of the magnetosphere: the entire Antarctic circle is on Earth's dark, leeward side, so no significant SH high-latitude geomagnetic flux is generated (Fig. 4), resulting in severely reduced SH SWIC strengths. It is also by no means coincidental that the 4 main SWIC loop centers lie roughly at 55° N/S, the boundary between the relatively productive (55-90°N, 55-90°S) and non-productive, low-angle geomagnetic inclination areas (55°N - 55°S).

Geo-SWIEM: Secular westward drift of the non-dipole field

For the past 150 years the non-dipole field has been shifting westward at an average rate of $0.18° a^{-1}$ (Merrill et al. 1998). This westward shift is easily explainable under the geo-SWIEM model: under the current "normal" polarity the SWICs run clockwise (when viewed from the north) around their circuits, and are therefore strongest in their east but lose energy as waste heat as they circuit to the west (Figs. 10-12). This relatively large heating of the eastern SWIC complex boundary over time results in a migration of the SWIC path – and its resultant non-dipole - to a cooler, lower-resistivity paths to the west (Fig. 10).

It is interesting in this regard that paleomagnetic declination data measured in Paris and modelled by CALS7K.2 (Gallet et al. 2003) demonstrate the eastward secular drifts of the magnetic pole between 900-1400 and 1600-1800 that roughly concur with dipole moment strengthening and Core cooling, while the westward secular NMP drifts between 1400-1600 and 1800-present correspond to dipole moment weakening and OC warming (Fig. 18). Yet the Paris data document a 20° shift in magnetic pole direction - not non-dipole location – and are likely more indicative of a geomagnetic excursion (see below). The Paris data do however document a strong link between magnetic pole drift and major solar cycles.

Geo-SWIEM: geomagnetic excursions

The non-dipole strength of the geomagnetic field is transient in nature: the field consists almost entirely of an inclined geocentric axial dipole (GAD) when averaged over super-millennial time periods (Merrill et al. 1998; Olson & Amit 2006). Intervals of stable geomagnetic field geometries with constant polarity are interrupted by magnetic reversals (rate: 2-3 per Ma), when the geomagnetic poles switch locations, as well as geomagnetic excursions (rate: 1 per 5-10 ka), when the magnetic pole directions significantly move away from the time-averaged dipole direction of the GAD (Gubbins 1999; Olson & Amit 2006). A spectrum of magnetic pole movements ranging from "large variation" (relatively common) to excursion (less common) to reversal (relatively uncommon) may exist, and the nomenclature becomes immaterial if the processes causing such variations are similar and known: a large variation may then also be termed a minor excursion, a strong excursion may grade into a failed reversal, etc.

A weakening of the dipole moment accompanies many excursions and reversals (Gubbins 1999; Olson & Amit 2006) suggesting the weakening of a coupled SWIC inductor pair is one possible cause of major magnetic pole movements. Recent data ([dataset]* NOAA 2021)

suggest that the geomagnetic field might currently be roughly halfway through a geomagnetic excursion: between 1900 and 1990 the Earth's dipole moment reduced from 8.29 to 7.84 10^{22} Am^2, and its NMP moved from near the North American SWIC complex center in 1900 to its current position near to the geographic north pole, that is to an intermediate position between the North American and Asian SWIC complex centers. If this movement continues, its current projected trajectory will cause the NMP to enter the Asian SWIC complex along its central meridian (100° E) en-route to its non-dipole center. This was explained previously by the weakening of the American SWIC pair, and the relative strengthening of the Asian-Madagascar pair. The current "large variation" requires these weakening/strengthening trends to continue for a true excursion to occur. Fig. 13a therefore represents a snapshot intermediary: what happens next will determine whether this 1900-2020 NMP "large variation" results in an excursion, and perhaps even a magnetic reversal.

Some of the earliest scientific observations suggest a geomagnetic excursion happened between 900-1100: Chinese scientists observed an increase in magnetic declination from -15° in 900 to 15° in 1100 (Smith & Needham 1967; note: declination sign reversed in order to be consistent to the CALS7K.2 model), and so documented an NMP excursion from the Asian SWIC complex to its North American counterpart. This shift is also very apparent in the Paris paleomagnetic declination data (Gallet et al. 2003) as well as CALS7K.2 declination animations (https://earthref.org/ERDA/432/ accessed 2022 June 13). However, this shift coincided with a dipole moment increase (Fig. 18), which is likely not fortuitous given that both phenomena are the result of the strength variance of coupled inductor pairs. The NMP shift and the increase in dipole strength are both consistent with a relative strengthening of the American SWIC pair over the period. A speculative explanation is therefore that during the waning stages of solar activity prior to the 900-1100 minimum (Fig. 18) the American circuits were able to cool more effectively than the Asian-Madagascar circuits, thereby reducing its their SWIC circuit resistivity, thereby relatively increasing their future SWIC circuit dipole moment contributions during the following solar minimum period, thereby tilting the NMP to the North American side.

Geo-SWIEM: geomagnetic reversals

Polarity reversal of a SWIC circuit can only occur when its dipole moment inverts due to a reversal of the SWIC flow direction, for example from its "normal" clockwise (when seen from the north) direction to a counterclockwise direction (Fig. 7). A number of possible current reversal sequences seem possible, though without more detailed geomagnetic reversal data such mechanisms must remain speculative. One plausible sequence is that a large geomagnetic excursion progresses to a magnetic reversal: a magnetic reversal is possibly the end-member of a spectrum of magnetic pole movements that includes variations and excursions (Gubbins 1999).

The analysis above indicated that the current NMP movement is likely the result of the weakening of the American SWIC inductor pair and the strengthening of the Asia-Madagascar coupled pair. Three intermediate sequence steps might separate this large variation from becoming a magnetic reversal:

The large variation could reverse if the weakening of the American SWIC pair reverses. In this scenario the cause of the North American SWIC circuit weakening could be an excessive heat build-up along their circuits, which could effectively be shed to the Mantle during

weaker SWIC periods. A renewed strengthening of the American pair would halt and possibly reverse the NMP progression. However, if the American SWIC pair weakens further then the large variation will become a geomagnetic excursion, while even further weakening could lead to the establishment of a North American negative non-dipole (Fig. 13 b).

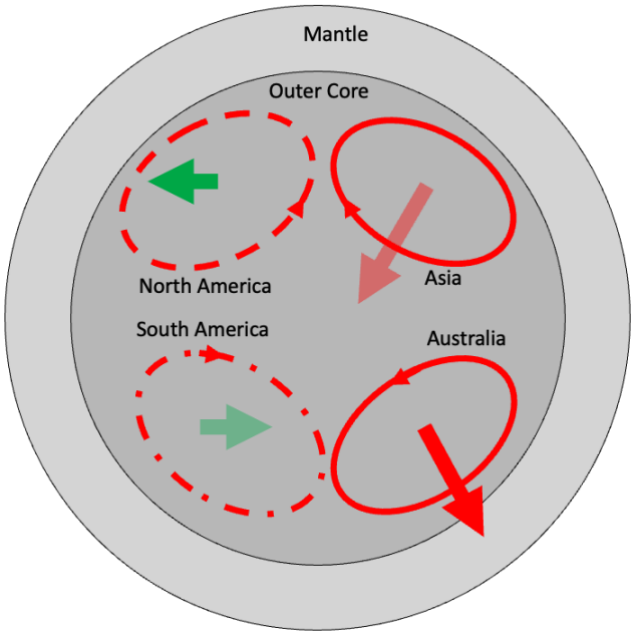

Figure 20: schematic of SWIC circuit couples during a magnetic reversal, whereby the left N-S inductor pairs switch to E-W inductor pairs, thereby reversing their SWIC current direction. Red loops represent SWIC circuits; solid lines are strong circuits, dashed lines induced circuits. Red arrows represent magnetic moments; green arrows induced magnetic moments. Not to scale.

The geomagnetic polarity cannot reverse – the NMP cannot progress further southwards - without a significant geomagnetic field geometry change. A tipping point is reached the moment the American pair (WH) no longer positively contribute to the global dipole, that is have weakened to the point where they are no longer have significant mutual induction, and are both acting as magnetic energy thieves from their EH counterparts (Fig. 20). In this scenario, the strong EH circuits increase their strength, while the weak WH circuits weaken further. The weakened American pair no longer form a mutual inductor pair, and progressively steal more energy from their eastern counterparts (Fig. 20), thereby forming E-W mutual inductor pairs with their EH counterparts, which reverses their circuit direction as well as their polarity (Fig. 20). The reversal of the American SWICs (counterclockwise flow) causes the geomagnetic field instability: “normal” polarity over the EH, “reverse” polarity over the WH. Dependent on whether the reversed American SWIC pair or the Asian pairs become strongest, the outcome will be a magnetic reversal or a failed reversal respectively.

The mechanisms above – while speculative – only rely on the relative strengthening and weakening of the coupled SWIC inductor pairs, whose centers – and magnetic moment directions – remain relatively constant during the entire process. Their combined magnetic moment vector – and the resultant Virtual Geomagnetic Pole (VGP) – will therefore always remain close to the 100° E & 90° W meridians that connect their non-dipoles. These magnetic reversal speculations are therefore supported by magnetic reversal VGP measurements: “transitional VGP paths are strongly biased to lie near the Americas or near an antipodal path” (McFadden & Merrill 1995; Gubbins & Love 1998; Merrill et al. 1998).

Geomagnetic Strength of a SWIC inductor loop

A SWIC circuit's magnetogenic efficiency was estimated to be 33%: the 4 TW of solar wind power that reaches the OC roughly creates 2.3 TW of heat and 1.7 TW of magnetic power. A SWIC circuit's radius varies (Fig. 17 bottom): the surface trace of the Asian loop increases from around 3500 km to the East, to 5000 km to the South, to over 6000 km in the west. Note that these radii need to be scaled by roughly 50% when projected back to the CMB. An average surface SWIC radius of 5000 km roughly equals 80% of the Earth's radius, so for the following calculations an average OC SWIC radius of 2750 km (≈0.8*3440km) is assumed. Further assuming an OC conductivity of 6 x 10^5 $S.m^{-1}$ (resistivity of 1.67 x 10^{-6} Ω.m; Merrill et al. 1998), and a (rather uncertain) OC magnetic permeability μ_C of 1.0 x 10^{-3} $N.A^{-2}$ (Ott 2009), the SWIC current I can be estimated as (Ohm's Law):

$$I = \sqrt{\frac{P}{R}} = \sqrt{\frac{(1.7)\,10^{12}\,W}{1.67\,10^{-6}\Omega.\mathrm{m}*2*\pi*2.75\,10^{6}m}} \approx 2.4 * 10^5\,A \qquad \text{(Eqn. 23)}$$

The average magnetic field strength, B_{avg}, can be estimated using the Biot-Savart law (Purcell & Morin 2013):

$$B_{avg} = \frac{\mu_C I}{2r} = \frac{1\,10^{-3}\left(\frac{N}{A^2}\right)(2.4)\,10^5\,A}{2*2.75\,10^6\,m} \approx 44000\,nT \qquad \text{(Eqn. 24)}$$

Note that this number should probably be reduced due to (outgoing) Mantle energy absorption: assuming A = 0.8 in Eqn. 1 leads to a B_{avg} = 35000 nT, which roughly equals the geomagnetic field strength at the equator between the Asian and Australian SWIC complexes (BGS 2021), and (ignoring the SANA) provides a surprisingly accurate estimate given the large number of rough estimates and uncertainties.

COMPARISON OF THE GEODYNAMO AND GEO-SWIEM MODELS

Evaluation of the geodynamo model

The Earth's magnetic field is commonly thought to be generated by a thermal geodynamo, whose OC convection cells convert thermal to magnetic energy via induced electric currents (Stanley 2014). A fairly recent review of 155 geodynamo models determined that the basic morphological properties of the geomagnetic field - relative axial dipole power, equatorial symmetry, zonality, and flux concentration - can only be reproduced under input parameters that are "remote from Earth's core values" (Christensen et al. 2010), that is the reviewed models can only produce Earth-like geometries using input parameters such as Core Ekman, magnetic Prandtl and Reynolds numbers, that are orders of magnitude different from realistic values. In fact, most models only focus on reproducing "accurate force balances even if the quantitative values for the parameters are not correct" (Stanley 2014). "Standard" dynamo models cannot reproduce (Christensen et al. 2010):

- The geomagnetic field strength: most models simulate non-dimensional field strength, and their realizations must be re-scaled
- The geographical locations of geomagnetic features and anomalies, such as the Earth's non-dipole anomalies
- Observed heat anomalies

- 4/6 magnetic field geometries of other planets, such as Saturn's highly axisymmetric magnetic field, or Mercury, Uranus and Neptune's offset dipole field, or Uranus and Neptune's non-axially dipolar fields (Stanley 2014).

Planetary dynamo models must assume:

- A wide range of existentially uncertain power sources, or a combination of such power sources, that differ from planet to planet, despite the fact that it is very unlikely that different dynamo configurations powered by a wide range of energy sources always generate simple, largely dipolar fields with magnetic axes roughly perpendicular to the planet's orbital plane.
- a slew of input parameters, such as Core Ekman, magnetic Prandtl and Reynolds numbers, that are orders of magnitude different from realistic values
- a self-exciting dynamo. A thermal or mechanical dynamo can only generate the necessary electric currents in a pre-existing magnetic field, which implies the dynamo must create itself, and recreate itself after magnetic reversals, as the OC is very likely above its Curie temperature and cannot retain a permanent magnetic field.
- The presence of a convecting liquid with a very high electrical conductivity (many dynamo models assume a conductivity approaching infinity), which is not a problem for Earth, but significantly strains credulity for proposed dynamos in Uranus' and Neptune's ionized water-ammonia-methane mantle, whose conductivity is likely several orders of magnitude lower than Earth's ferromagnetic core.
- A highly-modified dynamo model for Saturn's axisymmetric field: Cowling's anti-dynamo theorem demonstrates that a dynamo's fluid velocity vector and the magnetic field vector cannot both be axisymmetric, which implies that axisymmetric fields – such as Saturn's – cannot be modelled.

Dynamic dynamo models use a set of equations that balance Coriolis force, pressure, viscosity, gravity, and the Lorentz force, and should also include - but often omit - forces due to buoyancy and heat flows, which is problematic if these are the forces that are driving convection. The amount and geographical distribution of heat lost at the CMB should be one of the most fundamental boundary conditions constraining realistic geodynamo simulations.

Dynamo theory is unable to explain, and is often contradicted by, a large number of observations:

- Planetary magnetic field geometry unexplainable by "standard" dynamo theory, indicating its physical model needs major adjustments: 4/6 planets (Mercury, Saturn, Uranus, Neptune) and Ganymede
- Presumption of a speculative fluid magnetogenic source (fluid core or mantle layer) whose existence is solely indicated by the presence of a magnetic field: 4/6 planets (gas giants) and the Galilean satellites
- Demonstrably convecting fluids not generating a field: Venus
- No plausible internal energy source for heat anomalies: all planets
- Highly speculative magnetogenic energy sources, whose existence is solely indicated by the presence of a magnetic field: all planets and Ganymede:
    - No explanation: Jupiter, Uranus, Neptune
    - Negative buoyancy: Saturn, Ganymede
    - Positive buoyancy: Mercury, Earth

In summary: the speculative presence of a magnetogenic dynamo is used to hypothesize a wide range of speculative planet-internal power sources that through unclear processes generate highly similar dipolar magnetic fields.

The sole demonstrably-working planetary magnetogenic process is not a dynamo, as the sole non-speculative energy source - the magnetic flux generated by the Galilean satellites movement through Jupiter's tilted magnetic field - is planet-external, and is demonstrably generating the dipolar magnetic fields of Callisto, Europa and likely Ganymede via induction, a well-defined magnetogenic process based on the Maxwell equations (Zimmer et al. 2000; Collins & Johnson 2014)

Evaluation of the (geo-)SWIEM model

An alternative magnetogenic process – the geo-SWIEM – was derived from an integrated analysis of all relevant geomagnetic, geothermal, geologic and geoseismic data. This newly described OC process credibly simulates the strength and location of Earth's magnetic and heat anomalies, is plausibly responsible for most of the decennial to centennial surface-observed secular geomagnetic variability, and can be used to explain the magnetic field geometries and heat signatures of other planets (below). Furthermore, the described process is derived from the Maxwell equations, is physically far simpler that a thermal dynamo, and therefore more likely to reproduce the relatively simple planetary magnetic field geometries. The model requires no speculative assumptions, better reproduces observations, and has more predictive power than dynamo theory.

The recent review of 155 geodynamo models judged their ability to reproduce the basic morphological properties of the geomagnetic field - relative axial dipole power, equatorial symmetry, zonality, and flux concentration (Christensen et al. 2010). Using best-estimate input the geo-SWIEM model accurately reproduces:

- The Earth's relative axial dipole power (AD/NAD; axial/non-axial dipole ratio). Christensen et al. (2010) tested dynamo models against a representative value of 1.4. Fig. 9 indicates that the SWIC generated magnetic moments (vectors) can be resolved into axial and non-axial dipole components based on their moment angles. As the SWIC loops are centered around 55° latitude (Fig. 1), their AD/NAD = tan(55°) = 1.43, which matches the representative value.
- Equatorial symmetry. Fig. 9 demonstrates that equal strength SWICs generate equal strength magnetic moments. An equal strength NH-SH SWIC pair (Fig. 11) will generate equatorially symmetrical results.
- The actual geographical locations of geomagnetic features and anomalies, such as the Earth's non-dipole anomalies
- The Earth's average field strength.
- The Earth's heat anomalies

Note that Zonality and Flux concentration are at present difficult to evaluate, as they require a 3D geo-SWIEM model, but that neither are anticipated to present a significant problem.

THE MAGNETIC FIELDS OF OTHER PLANETS

Planetary Magnetic Field Strength

The previous analyses demonstrated that the geo-SWIEM model fairly accurately predicts the average geomagnetic field strength, which raises the question of how well it predicts the magnetic field strength of other planets. Dessler (1974) determines the Earth-incident solar wind power, U_s, as:

$$U_s = \pi\, r_M^2 \left(\frac{1}{2}\rho V_s^2 + \frac{B^2}{2\mu_0}\right) V_s \approx 5\ TW \qquad \text{(Eqn. 25)}$$

where r_M is the magnetosphere radius (assumed to be 12 Earth radii), ρ the mass density of the solar wind (8.10^{-21} kg.m^{-3} assumed), V_s the solar wind velocity (400 km.s^{-1} assumed), B the strength of the interplanetary magnetic field (IMF; assumed 10 nT), and μ_0 the magnetic permeability of free space ($1.26\ 10^{-6}$ H.m^{-1}). Note that the second term between the round brackets represents the incident magnetic energy of the IMF, which is commonly ignored as its size is much smaller than the first term, which represents the solar wind momentum energy. Table 2 presents the parameters that were used for the calculations.
Sources:

- solar wind & magnetospheres (Table 7.1 in Kivelson & Bagenal 2014)
- the planets' iron-rich core radii: Marley & Fortney 2014 (gas giants, Fig. 33.7 & 33.9), Murchie et al. 2014 (Mercury) and Merrill et al. 1998 (Earth). Note that Jupiter's C/Pl value was reduced from 0.06 (model) to 0.05 as this resulted in a perfect fit in Fig. 21 and its adjusted value is well within the range of Marley & Fortney's iterative gravitational model accuracy.

Planet	Radius Pl (Mm)	M/Pl	C/Pl	C (Mm)	Solar Wind ρ amu/cm^{-3}	v m/s	P TW	I kA	B_{calc} µT	B_0 µT
Mercury	2439	1.5	0.83	1951	60.000	500	0.2	51	**16.5**	**0.2**
Earth	6378	10	0.54	3441	8.000	500	6.4	247	**44.8**	**30.6**
Jupiter	71398	46	0.05	3570	0.300	500	637.0	2417	**423.2**	**430.0**
Saturn	60330	20	0.15	9050	0.100	500	28.5	322	**22.2**	**21.4**
Uranus	25559	25	0.13	3323	0.020	500	1.6	126	**23.7**	**22.8**
Neptune	24764	24	0.14	3715	0.008	500	0.6	72	**13.1**	**14.2**

Table 2: Comparison of Predicted (Bcalc) versus Observed (B0) Surface Magnetic Field at the Equator for the 6 Solar System planets showing an appreciable magnetic field. Pl: planet, M: magnetosphere, C: core, ρ: density, v: velocity, P: power, I: current intensity

Eqn. 23 was used to calculate the individual planet SWIC intensities (I) under assumptions identical to the previous section: a SWIC radius equal to 0.8 * the ferromagnetic core radius, core resistivity of 1.67×10^{-6} Ω.m, and a 33% efficiency of the solar wind power to magnetic power conversion. Mantle energy absorption was ignored. Eqn. 24 was then used to calculate the equatorial magnetic field strength of the planet under the assumptions of magnetic permeability μ_C of 1.0×10^{-3} N.A^{-2}. The method provides a remarkably good fit for the gas

giants (Fig. 21), a reasonable fit for Earth, and a remarkably poor fit for Mercury (not displayed). Fig. 21 clearly demonstrates that the SWIEM physical model has predictive power, and that the planetary magnetic field strengths show a strong correlation with average incident solar wind energy.

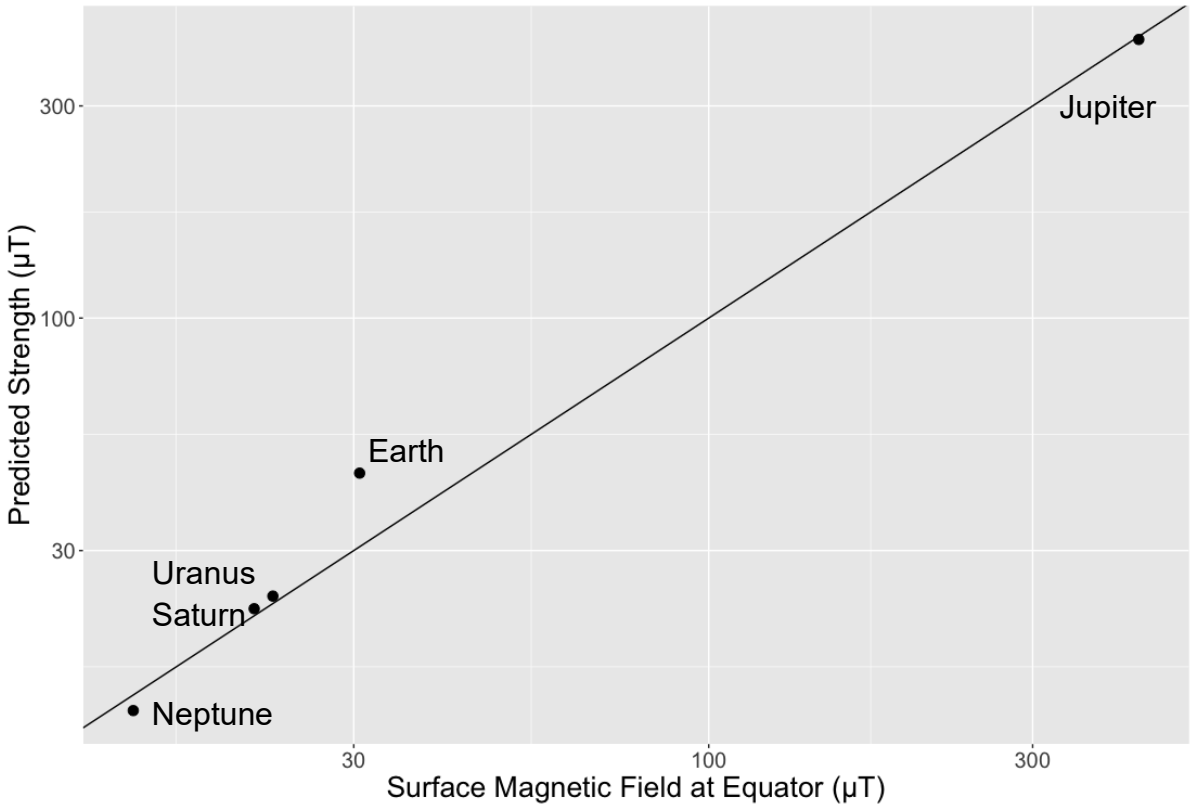

Figure 21: SWIEM-predicted versus observed planetary magnetic field strength. Note: Mercury (x=0.2; y=16.5) is not plotted. Note: logarithmic axes

Some comments:

- The method may require a different set of assumptions or equations to fit all planets equally well. For example, the cooling of the SWIC circuits may be far more efficient on the relatively cool gas giants than for Earth, where a radioactive Mantle generates significant heat (Stacey & Davis 2008).
- Earth is the only planet with plate tectonics, and as such may be the only planet where long-lived curvilinear heat anomalies guide the SWICs for prolonged time periods.
- The method is unsuitable for Mercury. Mercury has a 3:2 resonance orbit around the Sun (Dehant and Van Hoolst 2014), whereby the same side of the planet is facing the Sun for prolonged periods of time, and a sideral rotation period of 58.65 Earth days (Murchie et al. 2014): a Mercury solar day lasts 176 Earth days, thereby significantly limiting its diurnal magnetic flux (similar to Venus). It also has a very thin Mantle, and a core which comprises the bulk of the planet (Murchie et al. 2014). In addition, the Sun occasionally "backtracks" through Mercury's sky (Murchie et al. 2014), indicating Mercury is unique in its DSWGMF generation. Note that Mercury's weak field is also unexplainable under dynamo theory: "the dipole field is about two to three orders of magnitude weaker than that expected by scaling laws that estimate a dynamo-generated field's strength" (Stanley 2014).

Planetary Magnetic Fields and Heat Anomalies

The SWIEM model explains the great similarity (in essence more similar than dissimilar) between the magnetic fields of the planets: a highly conductive, highly magnetically permeable, fluid or solid ferromagnetic core, a low-conductivity, low magnetic permeable non-ferromagnetic mantle, and significant diurnal solar wind generated magnetic flux energy are the only requirements for a planetary magnetic field, which is the reason why most planets – and some moons - have one. Similar to Earth:

- the NH and SH SWICs in a planet's conductive core will initially flow to the same side of the planet
- the SWICs flow along the conductive core boundary towards the magnetic equator
- the NH and SH paired SWICs circuit back to their origin, thereby generating both external poloidal fields and internal toroidal fields
- Stronger SWIC circuits will generate greater dipole moments, and encircle positive non-dipoles. Weaker SWICs will cause negative non-dipoles due to mutual inductance.
- Ohmic heating along the circuit will cause core heating, which explains why some planets radiate more energy than they receive from high-frequency solar radiation alone: the solar wind induced currents cause Ohmic heating of the core, and part of this heat energy travels to the planet's surface where it is radiated to space. This Ohmic heating will be focused in the areas where the SWICs are strongest.

In contrast to Earth however the SWIC circuits on other planets are possibly not entrenched by steady-state heat anomalies, indicating these circuits may be more mobile, which in turn indicates that planetary magnetic field geometries may be significantly more variable than the geomagnetic field geometry. The solar wind diurnally deforms the magnetospheres of all planets, though large planets with shorter solar days (for example Jupiter) experience greater flux and induction effects - and therefore have stronger magnetic fields - than small planets with longer solar days (Mercury, Venus). Planets with longer orbits (Neptune, Uranus) show asymmetric magnetic fields, as their summer areas experience prolonged solar wind induction, causing a prolonged contrast in NH and SH SWIC strengths which likely limits or eliminates the coupled inductance between NH and SH SWIC circuits. The variability of the length of the planetary solar days and years, solar distance, rotational axes tilts, and planetary core radii therefore largely explain the variability of the planetary magnetic field geometries and strengths.

Saturn's Field

Saturn's proposed magnetogenic power source under dynamo theory - convection due to negative buoyancy of "Helium Rain" falling through the metallic hydrogen Mantle – is diffuse, highly speculative and likely orders of magnitude lower than its power requirements. In contrast, the Fig. 21 demonstrates that solar wind generated magnetic flux is a credible magnetogenic energy source that is able to explain Saturn's magnetic field strength. Saturn's magnetic field geometry cannot be explained under dynamo theory: its axisymmetric field geometry cannot be generated by a "standard" dynamo. Cowling's anti-dynamo theorem demonstrates that a dynamo's fluid velocity vector and the magnetic field vector cannot both be axisymmetric, which implies that axisymmetric fields – such as Saturn's – cannot be modelled (Merrill et al. 1998) In contrast, an axisymmetric field is the most easily-explained,

basic geometry under a SWIEM model: any axisymmetric SWIC circuit configuration will generate an axisymmetric geometry.

The easiest axisymmetric SWIEM configuration is one whereby a single NH / SH circuit pair are not entrenched, but rotate with the planet. Fig. 22 presents an alternative configuration, whereby 6 paired SWIC circuits generate an axisymmetric field geometry. A hexagonal north polar heat anomaly is generated during Saturn's northern summer, similar to that observed by Cassini's Composite Infrared Spectrometer (https://www.iflscience.com/that-giant-hexagon-at-saturns-north-pole-just-got-even-weirder-49644; Downloaded 22 September, 2022). During Saturn's northern summer its DSWGMF is maximal at its north pole (similar to Earth in Fig. 4), and therefore its NH SWICs are at maximum intensity. This has little effect on the Saturn's overall field geometry or strength, due to the coupled inductance of its NH and SH SWIC circuits, but does have an effect on its heat anomalies that will be maximal where the SWICs are strongest, that is at its north pole.

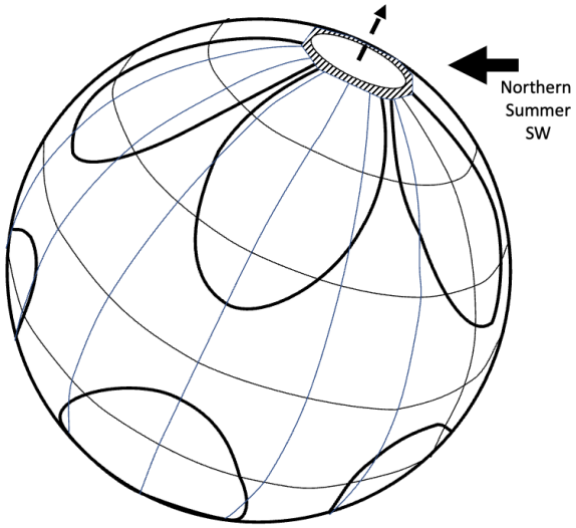

Figure 22: Schematic of a possible axisymmetric SWIEM geometry for Saturn. Solid lines represent notional SWIC circuits; hatched polar area represents hexagonal polar heat anomaly; dashed arrow is Saturn's magnetic axis.

Neptune's Field

Neptune's magnetic field cannot be explained under dynamo theory (Stanley & Bloxham 2004), and credible dynamo source layers and Neptune-internal heat sources are absent. That some internal heat source is active is irrefutable: Neptune radiates around 2.6 times the heat energy that it receives from high-frequency solar radiation (Pearl & Conrath 1991), which strongly implies that a large Neptune-external energy source – the solar wind – is increasing Neptune's internal energy. Neptune's magnetic field (Fig. 23) can be modelled as a magnetic dipole that shows a relatively large tilt of 47°, and is offset by a relatively large amount of 0.55 R_N (13500 km) from its center (Ness et al. 1989). Fig. 23 demonstrates that the SWIEM model is able to easily explain both Neptune's magnetic field geometry as well as its surface heat anomalies.

Neptune's year lasts 165 Earth years (Roman et al. 2022) indicating Neptune's seasons last over 41 years. Its southern summer solstice was in 2005 (Roman et al. 2022), so Neptune had just entered its SH summer at the time of the Voyager 2 flyby in 1989. During Neptune's

southern summer its DSWGMF is maximal at the south pole (similar to Earth's north pole in Fig. 4), and therefore its SH SWICs are at maximum intensity. Neptune's southern summer SWIEM geometry (Fig. 23) is dominated by strong SH SWICs that apparently have little coupled inductance with the far-weaker NH SWIC circuits, likely indicating the NH circuits are not defined by long-lived heat anomalies that can survive Neptune's long seasons. Neptune's rotational axis tilt is 28° (Fig. 23), so the SWIC generation model outlined in Fig. 9 must be rotated by a similar amount. The SWIEM model predicts that the strong SH SWICs generate a "reverse" field magnetic moment that is offset from Neptune's center, and is at a 45° angle to its rotation axis (Fig. 23), which almost exactly matches the observed 47° tilt (Ness et al. 1989). In addition, the model predicts significant heating occurs where the SWICs are strongest, that is at Neptune's south pole. Observations indicate Neptune's south pole temperature is currently hotter than the rest of the planet, and that its temperature peaked in 2005, during its summer solstice (Roman et al. 2022) indicating the SWIEM model also effectively explains Neptune's heat anomalies. Note that the SWIEM model predicts that Neptune's magnetic field and heat anomalies will be completely inverted during its northern summer in 2087.

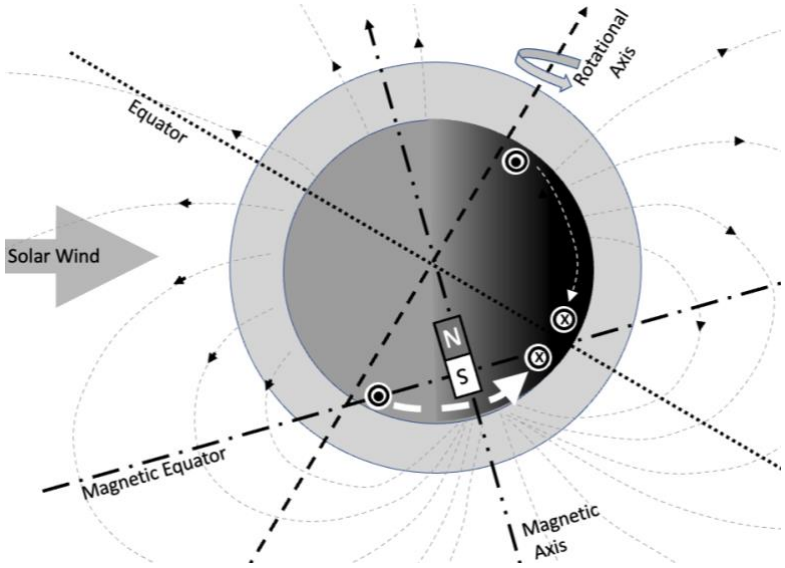

Fig. 23: Schematic of Neptune's magnetic field (after Ness et al. 1989). Thin dashed lines represent magnetic field lines; thick dashed line the rotational axis; dot-dash line the magnetic equator. Solid white arrows indicate SWIC circuits. Hatched ovals represent SWIC generation sweet-spots. Circled X's reflect electric circuit flow into the page; dotted circles electric circuit flow out of the page. Not to scale.

CONCLUSIONS

The Maxwell equations predict the existence of an Earth-internal solar-wind-powered-electromagnet, an Outer Core process that converts solar wind energy to geomagnetic energy and heat via electromagnetic induction. The newly proposed SWIEM model theorizes that a planet's magnetic field is largely powered by the solar wind's daily interactions with its magnetosphere. The model is an alternative to dynamo theory, and better explains the existence, magnitude and stability of the Earth's dipolar and non-dipolar fields, as well as its current polarity. It clarifies the origins of Earth's fluid Outer and solid Inner Core, and offers credible mechanisms for geomagnetic excursions and reversals, dipole strengthening and weakening, westward secular non-dipole drift, and the solar signals in the geomagnetic power spectrum. It accounts for the areas of high surface heat flux - such as plate margins and

hotspots - that originate in the Outer Core, and thereby establishes a credible link between the geomagnetogenic process and continental drift. The theory's underlying physical model can be used to explain the magnetic field geometry and heat anomalies of "problematic" planets such as Saturn and Neptune, and to accurately predict the equatorial magnetic field strengths of Earth, Jupiter, Saturn, Uranus and Neptune.

DATA ACCESSIBILITY

[dataset]* Deutsches Geoforschungszentrum (GFZ), 2021: Historical Geomagnetic Dipole moment CALS10k. https://www.gfz-potsdam.de/fileadmin/gfz/sec23/data/Models/CALSxK/DM_CALS10k_2.zip. Downloaded 2021 January 11.

[dataset]* Greg Kopp, 2019: Historical Total Solar Irradiation (TSI) data, https://spot.colorado.edu/~koppg/TSI/Historical_TSI_Reconstruction.txt. Downloaded 2021 January 11.

[dataset]* Morgan, W., Morgan, J., 2021, Plate velocities in hotspot reference frame: electronic supplement (http://www.mantleplumes.org/P%5E4/P%5E4Chapters/MorganP4ElectronicSupp1.pdf) Downloaded 2021 July 11

[dataset]* NOAA, 2021, (https://www.ngdc.noaa.gov/geomag/data/poles/NP.xy). Downloaded 2021 January 11

[dataset]* Service International des Indices Géomagnétiques (ISGI), 2021: aa index data, 1880-2020, http://isgi.unistra.fr/indices_aa.php. Downloaded 2021 January 11.

COMPETING INTERESTS

The author has no competing interests.

REFERENCES

Aubert, J., 2020, Recent geomagnetic variations and the force balance in Earth's core, *Geophysical Journal International*, **221**, 378–393 https://doi.org/10.1093/gji/ggaa007

Aubert, J., Finlay, C.C., 2019, Geomagnetic jerks and rapid hydromagnetic waves focusing at Earth's core surface. *Nat. Geosci.* **12,** 393–398. https://doi.org/10.1038/s41561-019-0355-1

Baker, D., Pulkkinen, T., Hesse, M., McPherron, R., 1997, A quantitative assessment of energy storage and release in the Earth's magnetotail. *JGR*, **102**, 7159-7168, doi: 10.1029/96JA03961.

Banerdt, W.B., Dehant, V., Grimm, R., GrOtt M., Lognonné, P., Smrekar, S.E., 2014, Probing the Interiors of Planets with Geophysical Tools. *In: Encyclopedia of the Solar System (Third Edition), Academic Press* ISBN: 978-0-12-415845-0, p. 1185-1203

Banks R.J., 1969, Geomagnetic Variations and the Electrical Conductivity of the Upper Mantle, *Geophys. J. R. Astr. Soc.*, **17**, 457-487.

BGS (British Geological Survey) 2021, The Earth's magnetic field: an overview. http://www.geomagnetism.bgs.ac.uk/education/earthmag.html Downloaded 16 August, 2021

Burke K., Plate Tectonics, the Wilson Cycle, and Mantle Plumes: Geodynamics from the Top. *Annu. Rev. Earth Planet. Sci*., **39**, 1–29, doi: 10.1146/annurev-earth-040809-152521

Chen, C. J., 2011, Physics of solar energy. Wiley, 370 pp. ISBN 978-0-470-64780-6

Christensen, U., Aubert, J., Hulot, G., 2010, Conditions for Earth-like geodynamo models, *Earth and Planetary Science Letters*, **296**, 487-496, doi://doi.org/10.1016/j.epsl.2010.06.009.

Collins, G., Johnson JT.V., 2014, Ganymede and Callisto. *In: Encyclopedia of the Solar System (Third Edition), Academic Press*, ISBN: 978-0-12-415845-0, p. 813-829

Connerny, J., Acuna, M., Hess, N., 1991, The Magnetic Field of Neptune., *J. Geophys. Res.*, 96, 19023-19042

Constable, C., Korte, M., Panovska, S., 2016, Persistent high paleosecular variation activity in southern hemisphere for at least 10 000 years. *Earth and Planetary Science Letters,* **453**, 78-86. 10.1016/j.epsl.2016.08.015.

Cowley, S. W. H., Bunce, E. J., and O'Rourke, J. M., 2004, A simple quantitative model of plasma flows and currents in Saturn's polar ionosphere, J. Geophys. Res., 109, A05212, doi:10.1029/2003JA010375, 2004b.

Crooker, N., Feynman, J., Gosling J. T., 1977, On the high correlation between long-term averages of solar wind speed and geomagnetic activity. *JGR,* **82**, 1933. doi:10.1029/JA082i013p01933

Currie, R.G., 1973, Geomagnetic line spectra-2 to 70 years. *Astrophys Space Sci*, **21**, 425–438, doi: 10.1007/BF00643106

Daglis, I. A., Thorne, R. M., Baumjohann, W., Orsini, S., 1999, The terrestrial ring current: Origin, formation, and decay, *Rev. Geophys*., **37**, 407– 438, doi:10.1029/1999RG900009.

De Michelis, P., Tozzi, R., Meloni, A., 2005, Geomagnetic jerks: observation and theoretical modeling. *Memorie della Società Astronomica Italiana*, **76,** 957–960

Dehant, V., Van Hoolst T., 2014, Rotation of Planets. *In: Encyclopedia of the Solar System (Third Edition), Academic Press.* ISBN: 978-0-12-415845-0, p 159-184

Dessler A., 1974, Some Problems in Coupling Solar Activity to Meteorological Phenomena. *Symp. Possible Relationships between Solar Activity and Meteorological Phenomena, Nov. 1973, NASA.*, 187-197

Eddy J., 1976, The Maunder Minimum. *Science*, **192**, 1189-1202

Ekström, G., Dziewonski, A.M., 1998, The unique anisotropy of the Pacific upper mantle. *Nature*, **394**: 168–172

Gallet, Y., Genevey, A., Courtillot, V., 2003, On possible occurrence of 'archaeomagnetic jerks' in the geomagnetic field over the past three millennia. *Earth and Planetary Science Letters*, **214**, 237-242, doi:10.1016/S0012-821X(03)00362-5.

Geological Survey of Canada, 2008, Tracking the North Magnetic Pole, http://www.matematicaescuola.it/materiale/fisica/campo_magnetico/Articoli/GSC North Pole.htm. Retrieved 11 January 2021.

Gosling J.T., 2014, The Solar Wind. *In: Encyclopedia of the Solar System (Third Edition), Academic Press* ISBN: 978-0-12-415845-0, p.261-279

Gubbins D., 1999, The Distinction between Geomagnetic Excursions and Reversals. *Geophys. J. Int*, **137**, F1-F3, https://doi.org/10.1046/j.1365-246x.1999.00810.x

Gubbins D., Love, J., 1998, Preferred VGP paths during geomagnetic polarity reversals: Symmetry considerations. *Geophysical Research Letters*, **25**, 1079–1082. doi:10.1029/98GL00711

Gubbins D., Alfè, D., Masters, G., Price, G.,Gillan, M.J., 2003, Can the Earth's dynamo run on heat alone?. *Geophysical Journal International*, **155**: 609-622. doi://doi.org/10.1046/j.1365-246X.2003.02064.x

Hamza, V. M., Cardoso, R. R., Ponte Neto, C. F., 2007, Spherical harmonic analysis of Earth's conductive heat flow. *Int J Earth Sci*, **97**, 205-226, doi: 10.1007/s00531-007-0254-3

Herman, J., Goldberg R., 1978, Sun, weather, and climate. *Scientific and Technical Information Office, NASA*

Khurana, K.K., Kivelson, M.G., Stevenson, D.J., Schubert, G., Russell, C.T., Walker, R.J., & Polanskey, C.A., 1998, Induced magnetic fields as evidence for subsurface oceans in Europa and Callisto. *Nature*, **395**,777-780.

Kivelson, M. G., Khurana, K.K., Russell, C.T., Volwerk, M., Walker, R.J., Zimmer, C., 2000, Galileo Magnetometer Measurements: A Stronger Case for a Subsurface Ocean at Europa. *Science*, **289**, 1340-1343

Kivelson, M.G., Bagenal, F., 2014, Planetary Magnetospheres *In: Encyclopedia of the Solar System (Third Edition), Academic Press*; ISBN: 978-0-12-415845-0, p. 137-157

Kushinov, A.V., 2008, 3-D Global Induction in the Oceans and Solid Earth: Recent Progress in Modeling Magnetic and Electric Fields from Sources of Magnetospheric, Ionospheric and Oceanic Origin. *Surv Geophys*, **29**, 139–186. https://doi.org/10.1007/s10712-008-9045-z

Le Mouël, J., Ducruix, J., Duyen, C., 1982, The worldwide character of the 1969-1970 impulse of the secular acceleration rate. *Phys. Earth Planetary Int.*, **28**, 337-350, doi: 10.1016/0031-9201(82)90090-5

Lühr, H., 2000, CHAMP Magnetic Field Recovery. http://op.gfz-potsdam.de/champ/science/magnetic_SCIENCE.html Retrieved 16 August, 2021

Marley, M.S., Fortney, J.J., 2014, Interiors of the Giant Planets. *In: Encyclopedia of the Solar System (Third Edition), Academic Press*, p. 743-758, ISBN: 978-0-12-415845-0

Matsushita, S. Maeda H., 1965, On the geomagnetic solar quiet daily variation field during the IGY. *JGR.* **70**, 2535–2558, doi: 10.1029/JZ070i011p02535

Mayaud P., 1972, The aa indices: A 100-year series characterizing the magnetic activity. *J. Geophys. Res*., 77(34), 6870-6874

McFadden, P., Merrill, R.T., 1995, Fundamental transitions in the geodynamo as suggested by paleomagnetic data, *Physics of the Earth and Planetary Interiors*, **91**, Pages 253-260, doi: 10.1016/0031-9201(95)03030-Z.

Merrill, R.T., McElhinny, M. W., McFadden, P. L., 1998, The magnetic field of the earth: paleomagnetism, the core, and the deep mantle. Academic Press. ISBN 978-0-12-491246-5.

Murchie, S.L., Vervack, R.J. Jr, Ernst, C.M., Strom, R.G., Mercury. *In: Encyclopedia of the Solar System (Third Edition), Academic Press*, ISBN: 978-0-12-415845-0, p. 283-304

Neish, C.D., Carter L.M., 2014, Planetary Radar. *In: Encyclopedia of the Solar System (Third Edition), Academic Press* ISBN: 978-0-12-415845-0, p. 1133-1158

Ness, N.F., Acuña, M.H., Burlaga, L.F., Connerney, J.E.P., Lepping, R.P.; Neubauer, F.M., 1989, Magnetic Fields at Neptune. *Science*. **246** (4936): 1473–78. doi:10.1126/science.246.4936.

NOAA, 2021, Major Magentic [sic] Storms 1868-2007 According to the AA* criteria https://www.ngdc.noaa.gov/stp/geomag/aastar.html. Retrieved 16 August 2021

Olson, P., Amit H. 2006, Changes in earth's dipole. *Naturwissenschaften.* **93**: 519–542 doi: 10.1007/s00114-006-0138-6

Purcell, E., Morin D., 2013, Electricity and Magnetism, Cambridge University Press, 839pp., ISBN: 9781107014022

Ott H.W. (2009) Electromagnetic Compatibility Engineering. John Wiley & Sons Inc., Hoboken. http://dx.doi.org/10.1002/9780470508510

Parkinson, W. D., 1983, Introduction to Geomagnetism, Scottish Academic Press, Edinburgh, ISBN: 0707302927, p. 308–340.

Pearl, J.C., Conrath, B.J., 1991, The albedo, effective temperature, and energy balance of Neptune, as determined from Voyager data. *Journal of Geophysical Research: Space Physics*. **96** (18) 921–30. doi:doi:10.1029/91ja01087.

Purcell , E.M., Morin D., 2013, Electricity and Magnetism, 3rd Edition, Cambridge University Press, ISBN 978-1-107-01402-2.

Roman, M.T., Fletcher, L.N., Orton, G.S., Vatant d'Ollone, J., Sinclair, J.A., Rowe-Gurney, N., Moses, J.I., & Irwin, P.J., 2020, Sub-Seasonal Variations in Neptune's Stratospheric Infrared Emission from VLT-VISIR, 2006-2018. The Planetary Science Journal, **3**, 41 pp, https://doi.org/10.3847/PSJ/ac5aa4

Ruff, L., Anderson D., 1980, Core formation, evolution, and convection: a geophysical model, Physics of the Earth and Planetary Interiors, **21**, 181-201, https://doi.org/10.1016/0031-9201(80)90069-2.

Schelkunoff S. A., 1943, EM Waves. Van Nostrand, New York, 530 pp.

Schultz M., 1991, The magnetosphere. *Geomagnetism*, **4**, 87-293, ISBN 0-12-378674-6

Smrekar, S.E., Stofan, E.R., Müller, N., 2014, Venus: Surface and Interior. *In: Encyclopedia of the Solar System (Third Edition), Academic Press* ISBN: 978-0-12-415845-0, p. 323-341

Smith, P., Needham, J., 1967, Magnetic Declination in Mediaeval China. *Nature* **214**, 1213–1214 https://doi.org/10.1038/2141213b0

Stacey, F., & Davis, P., 2008, Physics of the Earth (4th ed.). Cambridge: Cambridge University Press. doi:10.1017/CBO9780511812910

Stamper, R., Lockwood, M., Wild, M., Clark, T., 1999, Solar causes of the long-term increase in geomagnetic activity. *Journal of Geophysical Research*, **104,** 28325-28342. doi: doi.org/10.1029/1999JA900311

Stanley, S., 2014, Magnetic Field Generation in Planets. *In: Encyclopedia of the Solar System (Third Edition), Academic Press*, 121-135, ISBN: 978-0-12-415845-0

Stanley S., Bloxham, J., 2004, Convective-region geometry as the cause of Uranus' and Neptune's unusual magnetic fields. *Nature*. **428**(6979):151-3. doi: 10.1038/nature02376. PMID: 15014493.

Steinberger B., 2000, Plumes in a convecting mantle: Models and observations for individual hotspots. *Journal of Geophysical Research*. **105**. 11127-11152. https://doi.org/10.1029/1999JB900398.

Tkalčić, H., Phạm T., 2018, Shear properties of Earth's inner core constrained by a detection of J waves in global correlation wavefield. *Science*, **362**, 329-332, doi: 10.1126/science.aau7649

Turner, J. , Winch, D., Ivers, D., Stening, R., 2007, Regular daily variations in satellite magnetic total intensity data. *Annales Geophysicae,* **25**, 2167-2174.

Verhoogen, J., 1980, Energetics of the Earth. National Acad. of Sciences Collection, doi: 10.17226/9579

Weissman P.R., 2014, The Solar System and Its Place in the Galaxy. *In: Encyclopedia of the Solar System (Third Edition), Academic Press* ISBN: 978-0-12-415845-0, p. 3-28

Wu, C., Usoskin, I., Krivova, N., Kovaltsov, G., Baroni, M., Bard, E., Solanki, S., 2018, Solar activity over nine millennia: A consistent multi-proxy reconstruction. Astronomy & Astrophysics, **615**, 10.1051/0004-6361/20173

Zimmer, C., Khurana, K.K., Kivelson, M.G., 2000, Subsurface Oceans on Europa and Callisto: Constraints from Galileo Magnetometer Observations. *Icarus*, **147**, 329-347.